The Origin and Fate of Subantarctic Mode Water in the Southern Ocean

Article *in* Journal of Physical Oceanography · July 2021

DOI: 10.1175/JPO-D-20-0174.1

5 authors, including:

Zhi Li
Climate Change Research Centre
5 PUBLICATIONS **21** CITATIONS
SEE PROFILE

Ivana Cerovecki
University of California, San Diego
41 PUBLICATIONS **927** CITATIONS
SEE PROFILE

Yiyong Luo
Ocean University of China
51 PUBLICATIONS **544** CITATIONS
SEE PROFILE

JOBNAME: JPO 00#00 2021 PAGE: 1 SESS: 8 OUTPUT: Tue Aug 24 08:17:07 2021 Total No. of Pages: 22
/ams/jpo/0/jpoD200174

The Origin and Fate of Subantarctic Mode Water in the Southern Ocean

ZHI LI,[a,b] MATTHEW H. ENGLAND,[a,b] SJOERD GROESKAMP,[c] IVANA CEROVEČKI,[d] AND YIYONG LUO[e,f]

[a] *Climate Change Research Centre, University of New South Wales, Sydney, New South Wales, Australia*
[b] *Australian Research Council Centre of Excellence for Climate System Science, University of New South Wales, New South Wales, Australia*
[c] *Department of Ocean Systems, NIOZ Royal Netherlands Institute for Sea Research, Utrecht University, Texel, Netherlands*
[d] *Scripps Institution of Oceanography, University of California, San Diego, La Jolla, California*
[e] *Physical Oceanography Laboratory/CIMST, Ocean University of China, Qingdao, China*
[f] *Qingdao National Laboratory for Marine Science and Technology, Qingdao, China*

(Manuscript received 29 July 2020, in final form 23 June 2021)

ABSTRACT: Subantarctic Mode Water (SAMW) forms in deep mixed layers just north of the Antarctic Circumpolar Current in winter, playing a fundamental role in the ocean uptake of heat and carbon. Using a gridded Argo product and the ERA-Interim reanalysis for years 2004–18, the seasonal evolution of the SAMW volume is analyzed using both a kinematic estimate of the subduction rate and a thermodynamic estimate of the air–sea formation rate. The seasonal SAMW volume changes are separately estimated within the monthly mixed layer and in the interior below it. We find that the variability of SAMW volume is dominated by changes in SAMW volume in the mixed layer. The seasonal variability of SAMW volume in the mixed layer is governed by formation due to air–sea buoyancy fluxes (45%, lasting from July to August), entrainment (35%), and northward Ekman transport across the Subantarctic Front (10%). The interior SAMW formation is entirely controlled by exchanges between the mixed layer and the interior (i.e., instantaneous subduction), which occurs mainly during August–October. The annual mean subduction estimate from a Lagrangian approach shows strong regional variability with hotspots of large SAMW subduction. The SAMW subduction hotspots are consistent with the distribution and export pathways of SAMW over the central and eastern parts of the south Indian and Pacific Oceans. Hotspots in the south Indian Ocean produce strong subduction of 8 and 9 Sv ($1\,\text{Sv} \equiv 10^6\,\text{m}^3\,\text{s}^{-1}$) for the light and southeast Indian SAMW, respectively, while SAMW subduction of 6 and 4 Sv occurs for the central and southeast Pacific SAMW, respectively.

AU1 KEYWORDS: Southern Ocean; Entrainment; Ocean dynamics; Oceanic mixed layer; In situ oceanic observations; Seasonal variability

1. Introduction

Subantarctic Mode Water (SAMW) is a voluminous water mass formed on the equatorward side of the Antarctic Circumpolar Current (ACC) mainly by wintertime surface ocean heat loss and northward cross-frontal fluxes of cool, low-salinity surface water (Rintoul and England 2002). Both processes drive vigorous mixed layer convection in winter, forming thick layers of water with uniform density and thus low potential vorticity (PV) (McCartney 1977). The vertically homogeneous SAMW is then advected equatorward from the deep mixed layers at its formation location into the thermocline layer in the southern subtropical gyres, representing one of the major components of the upper limb of the global overturning circulation (Sloyan and Rintoul 2001). In this way, SAMW is ventilating and renewing the lower thermocline waters in all three Southern Ocean subtropical gyres (McCartney 1982; Hanawa and Talley 2001). SAMW thus plays a vital role in Earth's climate due to its ability to absorb carbon, oxygen, heat, and other properties from the atmosphere and transport them from the surface into the ocean interior (McCartney 1977, 1982; Iudicone et al. 2011; Roemmich et al. 2015; Gao et al. 2018).

The distribution and circulation of SAMW in the Southern Ocean have been quantified in past work (e.g., Wong 2005; Sallée et al. 2010a; Herraiz-Borreguero and Rintoul 2011, hereafter HBR11; Koch-Larrouy et al. 2011; Jones et al. 2016). AU2 Recent studies have further shown that SAMW has been undergoing significant changes over the Argo period in terms of its thickness, volume, and heat content (e.g., Roemmich et al. 2015; Gao et al. 2018; Kolodziejczyk et al. 2019; Meijers et al. 2019; Portela et al. 2020; Qu et al. 2020). In contrast, relatively little attention has been paid to the seasonality in SAMW and its formation. To gain a better understanding of the physical processes involved in altering SAMW, in this study we focus on the mechanisms controlling the seasonal evolution of SAMW. We further progress by splitting SAMW into its components within the mixed layer and in the ocean interior, providing an alternative basis for understanding the physical processes involved in the origin and fate of SAMW.

Deep Southern Ocean mixed layer convection due to wintertime air–sea buoyancy loss drives the subduction of SAMW from the mixed layer into the permanent pycnocline. The commonly used framework to estimate the net formation of SAMW in the Southern Ocean is a water-mass transformation framework (WMT; Walin 1982; Marshall et al. 1999; Nurser et al. 1999; Maze et al. 2009; Groeskamp et al. 2019xx). AU3 Previous studies using the WMT framework to study the formation of SAMW have demonstrated that the waters added by surface air–sea buoyancy fluxes and the waters mixed away by diapycnal mixing in the mixed layer and the interior are essential for SAMW variations (e.g., Sloyan and Rintoul 2001; Iudicone et al. 2008, 2011; Downes et al. 2011b; Kwon 2013;

Corresponding author: Zhi Li, zhi.li4@student.unsw.edu.au

DOI: 10.1175/JPO-D-20-0174.1

JOBNAME: JPO 00#00 2021 PAGE: 2 SESS: 8 OUTPUT: Tue Aug 24 08:17:07 2021 Total No. of Pages: 22
/ams/jpo/0/jpoD200174

Cerovečki et al. 2013; Evans et al. 2014, 2018; Portela et al. 2020). Annual mean WMT estimates driven by air–sea buoyancy fluxes range from 7.9 Sv (1 Sv $\equiv 10^6\,m^3\,s^{-1}$; Cerovečki and Mazloff 2016) up to 87 Sv (Karstensen and Quadfasel 2002b). This large range of SAMW formation rate estimates from the literature is difficult to compare, as different studies use different density ranges and air–sea flux products. Some studies suggest that ocean mixing and surface buoyancy fluxes lead to comparable WMT (Iudicone et al. 2008, 2011; Downes et al. 2011b; Cerovečki and Mazloff 2016). However, diapycnal transport due to small-scale turbulent mixing (de Lavergne et al. 2020) and mesoscale eddy mixing (Groeskamp et al. 2020) depends strongly on the choice of diffusivities used. Considering the complexities in calculating these diffusivities for an observational work, we only provide a rough estimate of the diapycnal transport/WMT due to these mixing processes. A detailed analysis of mixing is beyond the scope of this study; instead we focus on the effects of surface buoyancy loss on the formation of SAMW within the mixed layer.

The rates of WMT by air–sea buoyancy fluxes and ocean mixing that occur within two isopycnal surfaces and a fixed mixed layer base, would give the mass flux through the mixed layer base, referred to as the subduction rate (Marshall et al. 1999; Nishikawa et al. 2013). A more direct method to compute SAMW subduction is to use a kinematic approach that estimates the rate at which fluid passes between the surface mixed layer and the ocean's interior (Marshall et al. 1999), either from an Eulerian viewpoint (Cushman-Roisin 1987; Williams 1991; Marshall et al. 1993) or from a Lagrangian viewpoint (Woods 1985; Qiu and Huang 1995). The associated SAMW subduction rate estimates also have a wide range, from 7 Sv (Sallée et al. 2010a) to more than 100 Sv (Downes et al. 2010; Liu and Huang 2012; Liu and Wang 2014), suggesting that the SAMW subduction process is still not fully understood. This is partly because, of the water that is subducted, a certain portion can be reentrained back into the mixed layer further downstream in the ACC (Woods 1985; Marshall et al. 1993; Qiu and Huang 1995). In addition, of the water that subducts and moves north from the ACC into the subtropical gyres, a certain portion can reenter the Southern Ocean as "old" SAMW via poleward flowing western boundary currents, after completing a circuit of the southern subtropical gyres (Wong 2004; Ridgway and Dunn 2007; Iudicone et al. 2008). Both the reentrainment and the return of old SAMW are not accounted for in our subduction calculation, as we focus on the SAMW formation by the subduction process. In contrast, the WMT approach accounts for both the reentrainment and the return of old SAMW in its estimate of the total SAMW formation rate.

Variations in the mixed layer depth (MLD) affect the rate of exchange between the surface mixed layer and the ocean interior (Sallée et al. 2010a). Due to the north–south migration of solar radiation, seasonal buoyancy forcing induces a large seasonal cycle in the Southern Ocean mixed layer (Sallée et al. 2010b; Dong et al. 2008) and thus, the subduction of SAMW. Previous studies have shown the important role of adiabatic subduction and diabatic WMT processes by surface buoyancy fluxes and diapycnal mixing in the seasonal cycle of SAMW (e.g., Kwon 2013; Kwon et al. 2013; Evans et al. 2014, 2018; Cerovečki and Mazloff 2016). While the above studies have advanced our understanding of the mechanisms controlling SAMW variability, there have been relatively few studies that directly reconcile volumetric changes of SAMW with SAMW formation mechanisms on monthly time scales. The first goal of this study is to extend the analysis of the seasonal cycle of SAMW formation by comparing subduction and air–sea formation rates with the volumetric changes in SAMW. Importantly, we separately consider the annual cycle of the SAMW volume both within the mixed layer and in the ocean interior in order to examine the exchange between these two volumes. Combining the volume changes of mixed layer and interior SAMW with mechanisms connecting the surface mixed layer with the ocean interior provides new insights into understanding the formation of SAMW. Another goal is to extend on past work by calculating the annual mean subduction by applying the Lagrangian method and SAMW volume transport at previously defined hotspots of SAMW formation (Sallée et al. 2010a; HBR11; Jones et al. 2016; Kolodziejczyk et al. 2019).

The hydrographic data used in this study are described in section 2. We identify SAMW and examine its climatological mean spatial distribution in section 3. The annual mean subduction rates are then estimated using a Lagrangian framework, focusing on the formation hotspots and the export of SAMW (section 4). Kinematic subduction estimates are then combined with the SAMW surface formation rate estimates due to air–sea buoyancy fluxes (section 5) to understand observed climatological volume changes of SAMW (section 6). A rough estimate of the role of ocean mixing is provided using a volumetric budget analysis of waters within the SAMW layer in section 7. Last, we provide a summary of our findings in section 8.

2. Hydrographic data

The Roemmich–Gilson Argo data from January 2004 to September 2018 [Roemmich and Gilson (2009), and updates thereafter; hereafter referred to as RG09] have been used to calculate SAMW volume and its changes. RG09 is a gridded dataset of monthly averaged in situ temperature and practical salinity, using data only from Argo floats. The data are provided on 58 pressure layers (2.5–1975 dbar) on a 1° × 1° horizontal resolution from 64.5°S to 79.5°N. First, RG09 data are recalculated to Conservative Temperature (Θ, McDougall 2003) and Absolute Salinity (S_A; McDougall et al. 2012) using the GSW Oceanographic Toolbox (IOC et al. 2010). Then, we apply a vertical stabilization software (Barker and McDougall 2017) to stabilize the monthly data, to ensure that the ocean is stably stratified on time scales of months. Then the surface-referenced potential density σ_0 and neutral density γ^n are calculated. The average number of Argo profiles per 1° box is about 48 in the Southern Ocean (30°–65°S) with most of them residing on the equatorward side of the Subtropical Front (Fig. 1a).

The horizontal velocity is obtained from the thermal-wind relation by assuming a level of no motion at 1950 m. As a true "level of no motion" does not actually exist, we repeat calculations using observationally based estimates of geostrophic velocity at 1950 m

JOBNAME: JPO 00#00 2021 PAGE: 3 SESS: 8 OUTPUT: Tue Aug 24 08:17:07 2021 Total No. of Pages: 22
/ams/jpo/0/jpoD200174

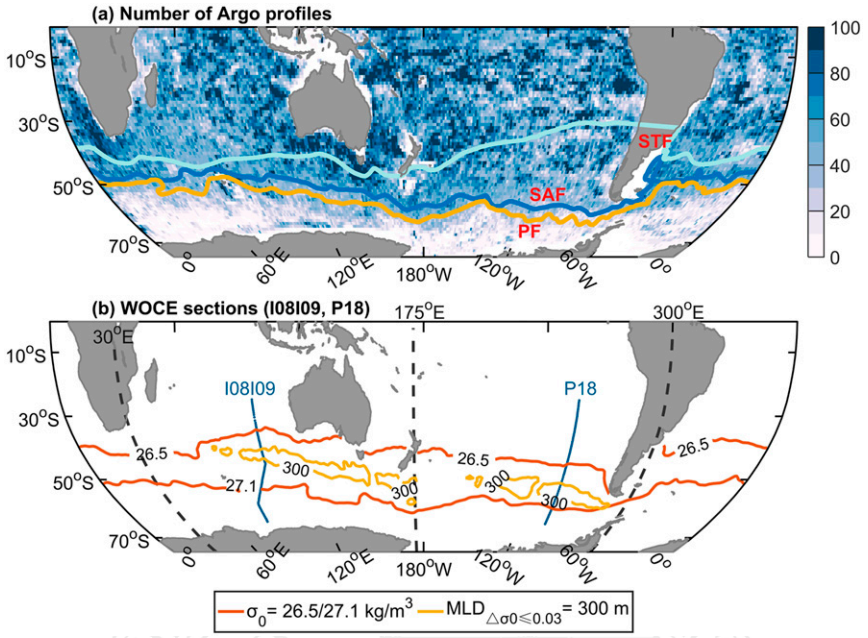

FIG. 1. (a) The number of Argo profiles per 1° box (shading) collected by the Argo Program (www.argo.ucsd.edu) up until August of 2019. The climatological positions of the Subtropical Front (STF, light blue), Subantarctic Front (SAF, dark blue), and Polar Front (PF, yellow) are taken from Orsi et al. (1995). (b) Blue lines represent the position of hydrographic sections from the World Ocean Circulation Experiment (WOCE) at ~82°–95°E (I08I09) and ~103°W (P18). Red lines represent the positions of isopycnals σ_0 = 26.5 and 27.1 kg m^{-3} at 10-m depth in September from the RG09 Argo product. Yellow contours indicate the 300-m depth of the maximum winter mixed layers from the climatological year of RG09. Superimposed black dashed lines indicate the longitudes 30°E, 175°E, and 60°W, which are used to divide the Southern Ocean into three basins: the Indian (30°–175°E), Pacific (175°E–60°W), and Atlantic Oceans (60°W–30°E), respectively, all south of 30°S.

taken from Gray and Riser (2014) and at 1000 m from Lebedev et al. (2007), respectively, to get a full-depth geostrophic velocity field. The geostrophic velocity presented in this paper uses the mean of these three derived velocity fields.

The Θ and S_A fields from RG09 are combined with the monthly air–sea buoyancy fluxes from the European Centre for Medium-Range Weather Forecasts (ECMWF) Reanalysis Interim (ERA-Interim), to estimate the surface water-mass transformation rate in the SAMW density range. The horizontal wind stress vectors $\boldsymbol{\tau}$ for the period 2004–18 are also taken from ERA-Interim to estimate Ekman pumping velocity, $w_{EK} = \text{curl}(\boldsymbol{\tau})/(\rho_0 f)$, where f is the planetary vorticity and ρ_0 is used as the surface-referenced potential density, $\rho_0 = \sigma_0 + 1000\,\text{kg m}^{-3}$, at 10-m depth. Combining the RG09 hydrographic data with ERA-Interim, the monthly climatology can resolve the seasonal cycle of SAMW variability and provide relatively robust observational-based estimates of the climatological subduction and surface water-mass formation rate.

3. SAMW definition and distribution

a. *The SAMW identification*

Moving around the circumpolar Southern Ocean, winter mixed layers (Fig. 1b) contain distinctly varying SAMW pools with different temperature and salinity (HBR11; Meijers et al. 2019; Cerovečki et al. 2019; Tamsitt et al. 2020). The density of SAMW increases from ~26.5–26.8 kg m^{-3} in the central Indian Ocean up to ~26.9–27.1 kg m^{-3} in the east Pacific Ocean (Fig. A1g), due to freshening and cooling of SAMW (McCartney 1977; Wong 2005; Dong et al. 2008). Because the change in density affects PV, we separately determine the PV and density criteria for identifying the local modes of SAMW in the main SAMW formation regions.

Considering the volume of low PV water as a function of density for each ocean sector (Fig. A1) shows that in the Indian Ocean, low PV (PV ≤ 8×10^{-11} m^{-1} s^{-1}) SAMW can be found in the density range σ_0 = [26.5–27.0] kg m^{-3}, Absolute Salinity range S_A = [34.4–35.6] g kg^{-1}, and Conservative Temperature range Θ = [4–15]°C. Here, potential vorticity is defined as PV = $(f/\rho_0)\partial\rho_0/\partial z$, where z is the water depth. In the Pacific Ocean, low PV (PV < 7×10^{-11} m^{-1} s^{-1}) SAMW is found in the range of σ_0 = [26.6–27.1] kg m^{-3}, S_A = [34.2–35.2] g kg^{-1}, and Θ = [4–14]°C. The Atlantic SAMW is identified using the same criteria as in the Indian Ocean. All the criteria we apply to identify SAMW are summarized in Table 1. Detailed descriptions of the SAMW identification can be found in appendix A. Note in this study we define the SAMW density range as the potential density criteria given in Table 1. We additionally impose the PV, temperature, and salinity constraints from Table 1

JOBNAME: JPO 00#00 2021 PAGE: 4 SESS: 8 OUTPUT: Tue Aug 24 08:17:08 2021 Total No. of Pages: 22
/ams/jpo/0/jpoD200174

TABLE 1. Definition of SAMW used in the text. Acronyms and symbols: potential vorticity (PV), surface-referenced potential density (σ_0), Conservative Temperature (Θ), Absolute Salinity (S_A), and neutral density (γ^n). The Atlantic SAMW is identified using the same criteria as in the Indian Ocean.

	PV (10^{-11} m^{-1} s^{-1})	σ_0 (kg m^{-3})	Θ (°C)	S_A (g kg^{-1})	γ^n (kg m^{-3})
Indian (30°–175°E)	≤8	26.5–27.0	4–15	34.4–35.6	26.54–27.12
Pacific (175°E–60°W)	≤7	26.6–27.1	4–14	34.2–35.2	26.66–27.25

when calculating the SAMW thickness, volume, and transport, as well as when calculating the SAMW formation by subduction in sections 3–6. The PV, temperature, and salinity constraints in Table 1 are also included in the estimate of SAMW formation by air–sea buoyancy fluxes (sections 5 and 6). Since the water-mass formation is derived as the convergence of WMT [Eq. (D2)], a fixed density range over the circumpolar Southern Ocean is needed to first estimate the WMT and then get the formation rate over the SAMW density range. Here we use a fixed density range of σ_0 = [26.5–27.1] kg m^{-3} in order to encompass the SAMW density ranges in all Southern Ocean sectors. Therefore the estimate of SAMW formation by air–sea buoyancy fluxes has a slight mismatch with the SAMW definition used for other calculations, but can still be used for this comparison exercise.

b. Spatial distribution of deep mixed layers and SAMW

Mixed layer depth is defined as the depth at which σ_0 is 0.03 kg m^{-3} greater than the value of σ_0 at 10-m depth (de Boyer Montégut et al. 2004). Deep wintertime mixed layers, indicated by white contours in Fig. 2a, mainly reside in the region extending from the southwest of Australia to south of New Zealand, and in the southeast Pacific Ocean from 160°W to the Drake Passage (Dong et al. 2008).

The SAMW thickness (Fig. 2b) estimated using the definition in section 3a resembles that shown in Gao et al. (2018). SAMW lies only on the north side of the Subantarctic Front. SAMW thickness can be up to ~600 m in vertical extent, from the surface at subduction regions to the intermediate layer (Fig. 2), with a maximum of ~800 m seen just east of New Zealand. Thick SAMW layers match up with regions of deep mixed layers, in which the low PV mixed layer waters are subducted into the ocean interior during winter (Fig. 2). Meridional PV transects across the region of the deepest wintertime mixed layers indicate that the thickness of the low PV layer decreases due to mixing processes along the export pathway toward the equator (Figs. 2c,d) (HBR11; Kolodziejczyk et al. 2019; Portela et al. 2020).

4. Kinematic estimate of subduction rate

In this section, we estimate SAMW formation by subduction using a kinematic approach and investigate its regional variability.

a. Background theory

Subduction can be thought of as an injection of fluid from the surface mixed layer into the ocean interior (Cushman-Roisin 1987). Its counterpart, commonly referred to as obduction, involves an injection of water from the ocean interior back into the mixed layer. These processes couple the dynamics of the mixed layer with the ocean interior.

To estimate the volume flux entering the ocean interior, an Eulerian approach has been widely used (Cushman-Roisin 1987; Williams 1991; Marshall et al. 1993). Here the instantaneous subduction rate (S^E) can be expressed as

$$S^E = \frac{\partial h}{\partial t} + \mathbf{u}_h \cdot \nabla h + w_h, \tag{1}$$

where h is the depth of the mixed layer, $\partial h/\partial t$ is the time rate of MLD change, $\mathbf{u}_h \cdot \nabla h$ represents the lateral advection of fluid through the sloping base of the mixed layer (Fig. 3a), and w_h is the vertical velocity at the mixed layer base. Subduction ($S^E > 0$) represents detrainment from the mixed layer into the underlying fluid column. In contrast, obduction ($S^E < 0$) involves entrainment from the underlying column of water into the surface mixed layer.

Although detrainment takes place over a long period of the seasonal cycle, only the water parcels that originate during the effective subduction period, when the mixed layer reaches its annual maximum and starts to retreat, can irreversibly penetrate into the permanent pycnocline (Marshall et al. 1993; Qiu and Huang 1995). Detrainment can also occur outside of this period, but the detrained parcels are only temporarily detrained into the seasonal pycnocline and will eventually be reentrained back by a deepening mixed layer over the subsequent months. By defining the effective subduction period, the annual mean subduction rate (S^E_{ann}) can be written as (Marshall et al. 1993)

$$S^E_{\text{ann}} = \frac{1}{T}\int_{T_s^S}^{T_e^S} S^E(t)\, dt. \tag{2}$$

Here T is one year, and T_s^S and T_e^S are the times when effective detrainment starts and ends. The term $S^E(t)$ can be defined by the kinematic relation Eq. (1) (Marshall et al. 1993), so that Eq. (2) can be rewritten as

$$S^E_{\text{ann}} = \frac{1}{T}\int_{T_s^S}^{T_e^S}\left(w_{\text{EK}} - \frac{\beta}{f}\int_{-h}^{0} v_m\, dz + \mathbf{u}_h \cdot \nabla h\right) dt + \frac{1}{T}\left(h_{T_e^S} - h_{T_s^S}\right), \tag{3}$$

where $h_{T_s^S}$ and $h_{T_e^S}$ are the MLD at the beginning and at the end of the effective subduction period, respectively. The vertical component w_h in Eq. (1) is replaced by Ekman pumping (w_{EK}), and subsequently gets corrected for its contribution to the meridional Sverdrup transport within the mixed layer (Marshall et al. 1993), namely $w_h = w_{\text{EK}} - (\beta/f)\int_{-h}^{0} v_m\, dz$, where β is the meridional gradient of f, and v_m is the meridional velocity within the mixed layer.

Since the detrained waters from the mixed layer base can be viewed as being advected by geostrophic velocities along an

JOBNAME: JPO 00#00 2021 PAGE: 5 SESS: 8 OUTPUT: Tue Aug 24 08:17:08 2021 Total No. of Pages: 22
/ams/jpo/0/jpoD200174

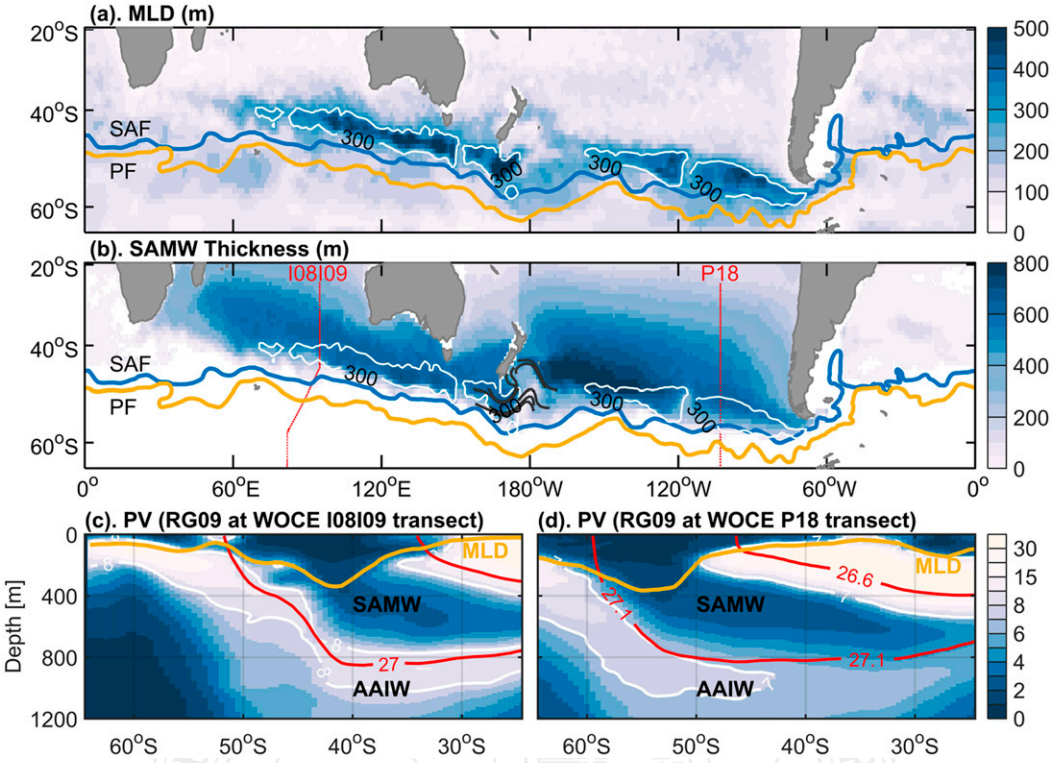

FIG. 2. Horizontal distribution of (a) the maximum MLD (m) and (b) the annual mean thickness (m) of SAMW. Blue and yellow bold contours are as in Fig. 1a. White thick contours represent 300-m depth of the maximum MLD from the monthly climatological mean of RG09. The MLD here is defined as the depth at which σ_0 has increased by 0.03 kg m^{-3} relative to 10 m (de Boyer Montégut et al. 2004; Dong et al. 2008). Red dots show the position of the WOCE transects I08I09 and P18, as shown in Fig. 1. Black lines in (b) indicate some Lagrangian trajectories of the subducted SAMW around the Campbell Plateau (170°E) taken from Fig. 3b. (c),(d) Monthly mean potential vorticity ($\times 10^{-11}$ m^{-1} s^{-1}; color) in September as a function of depth and latitude on the location of WOCE hydrographic sections I08I09 at ~82°–95°E in (c) and P18 at ~103°W in (d), shown as blue lines in Fig. 1b and red lines in Fig. 2b. Here, the superimposed red (white) solid lines show isopycnals (PV isolines) for values used as a threshold to identify the SAMW in these two sections. Yellow solid line shows the MLD in September. All data are obtained from the RG09 Argo product for 2004–18 and interpolated to the location of the WOCE transects.

isopycnal surface, Woods (1985) and Qiu and Huang (1995) suggested an alternative approach. Namely, that the annual subduction rate (S^L_{ann}) can be estimated by tracking water parcels released at the base of the mixed layer in September for one year in a Lagrangian framework:

$$S^L_{\text{ann}} = -\overline{\left(w_{\text{EK}} - \frac{\beta}{f}\int_{-h_m}^{0} v_m\, dz\right)} + \overline{\mathbf{u}_m \cdot \nabla h_m} + \overline{\frac{\partial h}{\partial t}}$$

$$= \underbrace{-\overline{\left(w_{\text{EK}} - \frac{\beta}{f}\int_{-h_m}^{0} v_m\, dz\right)}}_{\text{vertical}} + \underbrace{\frac{1}{T}(h_{m,0} - h_{m,1})}_{\text{lateral}}, \qquad (4)$$

where $h_{m,0}$ and $h_{m,1}$ denote the MLD at the initial and final locations, respectively. The overbar indicates an average over the pathway of the one-year Lagrangian trajectory (Fig. 3b). The first two terms on the right side of Eq. (4) denote the contribution of vertical pumping at the base of the mixed layer, and the third term, referred to as lateral advection, represents the contribution due to spatial variations in MLD following a Lagrangian parcel (Fig. 3a). This Lagrangian approach enable us to estimate the annual mean transfer of fluid from the mixed layer to the permanent pycnocline. Grid points with negative values (i.e., no subduction) are omitted in this calculation. A Runge–Kutta fourth-order method has been applied to the velocity interpolations to obtain more reliable Lagrangian trajectories.

b. *Defining input variables*

The Lagrangian subduction rate estimates require calculations of the MLD and geostrophic velocities. We use the MLD definition given in section 3b and horizontal velocities as described in section 2. To test the uncertainties in subduction rate that originate from our choices in MLD and velocity fields, we perform a sensitivity test for different MLD criteria, which involves testing density criteria for MLD of $\Delta\sigma_0 \le 0.03$ kg m^{-3} and $\Delta\sigma_0 \le 0.125$ kg m^{-3}, and different reference velocity fields (see appendix B). These MLD and velocity fields yield

JOBNAME: JPO 00#00 2021 PAGE: 6 SESS: 8 OUTPUT: Tue Aug 24 08:17:08 2021 Total No. of Pages: 22
/ams/jpo/0/jpoD200174

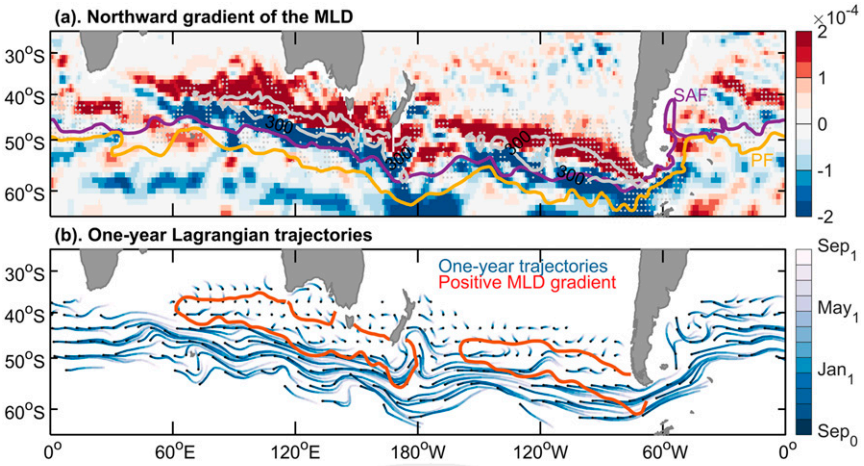

FIG. 3. (a) Meridional gradient of MLD in September (shading). Positive indicates northward shallowing of the mixed layer. Gray dots represent the grid points with MLD shoaling eastward coinciding with positive eastward flow at the mixed layer base. Superimposed are climatological positions of the Subantarctic Front (purple) and Polar Front (yellow) taken from Orsi et al. (1995), respectively. (b) One-year Lagrangian trajectories of SAMW particles in the Southern Ocean released at the base of the September mixed layer. Only the subducted particles ($S^L_{\text{ann}} > 0$) are considered. The color of the trajectory changes from dark blue at the start point (black dots) toward light blue at the ending point. Red contours indicate the area with large northward positive gradients of MLD shown in (a).

essentially the same subduction pattern and year-to-year variability (Fig. B2), suggesting the robustness of the results obtained in our study.

Previous studies have pointed out that the eddy-induced subduction rate is comparable in magnitude to the subduction rate induced by the mean flow (Sallée et al. 2010a; Sallée and Rintoul 2011; Hiraike et al. 2016; Portela et al. 2020). However, the eddy-induced flow and subduction depend strongly on the choice of eddy-diffusion coefficient (Sallée and Rintoul 2011; Hiraike et al. 2016; Canuto and Cheng 2019; Groeskamp et al. 2016, 2020). This degree of analysis is beyond the scope of this study. Besides, the instantaneous subduction related to MLD variations ($\partial h/\partial t$) dominates Eq. (1) (see section 6 and also Kwon 2013). Therefore, in this study, we focus on the subduction induced by geostrophic mean flow.

c. *Total SAMW subduction rate*

We now use the Lagrangian approach [Eq. (4)] to estimate fields of the annual mean subduction rate of SAMW. The integrated SAMW subduction rates after imposing the SAMW constraints (provided in section 3a and Table 1) are 27.3, 11.4, and 3.4 Sv over the Indian (30°–175°E), Pacific (175°E–60°W), and Atlantic (60°W–30°E) Oceans, respectively (Fig. 4a). The subduction rate estimates are binned into 0.1 kg m^{-3} density bins (Fig. 5a), and the values provided are within the range of subduction rate estimates from previous studies (e.g., Karstensen and Quadfasel 2002a,b; Downes et al. 2009, 2010, 2011a; Liu and Huang 2012; Liu and Wang 2014; Qu et al. 2020). The resulting subduction rates vary significantly across ocean basins, with most subduction occurring from the central Indian Ocean to the southeast Pacific on the equatorward side of the Subantarctic Front. Furthermore, the subduction of SAMW in the Indian Ocean is about twice that in the Pacific Ocean, whereas the Pacific SAMW has a larger volume (Figs. A1a,g and Figs. 4g–i and 5). This is likely due to newly subducted SAMW in the Indian Ocean that is transported toward the Pacific along the ACC (Jones et al. 2016; Lu et al. 2020, manuscript submitted to *Nat. Commun.*), as seen from the Lagrangian trajectories around the Campbell Plateau (170°E; Figs. 2b and 3b). Some of the Indian SAMW may be obducted back into the mixed layer, while some may remain as the subducted mode water. As such, the Pacific SAMW likely contains a substantial component of Indian SAMW, especially east of New Zealand to 160°W (Fig. 2b).

The Lagrangian subduction given by Eq. (4) is comprised of the lateral advection (Fig. 4b) and vertical pumping (Fig. 4c). The contribution from lateral advection (~80%) is approximately 4 times larger than that of vertical pumping (~20%). The positive contribution from the vertical pumping to subduction is mainly restricted to the northern side of the Subantarctic Front in the Indian Ocean and central Pacific (Karstensen and Quadfasel 2002b; Sallée et al. 2010a).

The lateral advection is strong in the regions of deep mixed layers with relatively large horizontal MLD gradients (Figs. 3a and 4b), such as north of the ACC in the central and eastern parts of the south Indian and Pacific Oceans (Fig. 4b). The 1-yr Lagrangian trajectories (Fig. 3b) and the interior PV structure on the isopycnal surfaces (Figs. 4d–f) would suggest that branches of subducted water are advected from the northern limit of the ACC to join the subtropical gyre circulation, such as from the regions 60°–100°E to the northeast of the Kerguelen Plateau, 120°–140°E to the west of Tasmania, and 150°–80°W north of 55°S. In this way, the northward component of lateral

JOBNAME: JPO 00#00 2021 PAGE: 7 SESS: 8 OUTPUT: Tue Aug 24 08:17:08 2021 Total No. of Pages: 22
/ams/jpo/0/jpoD200174

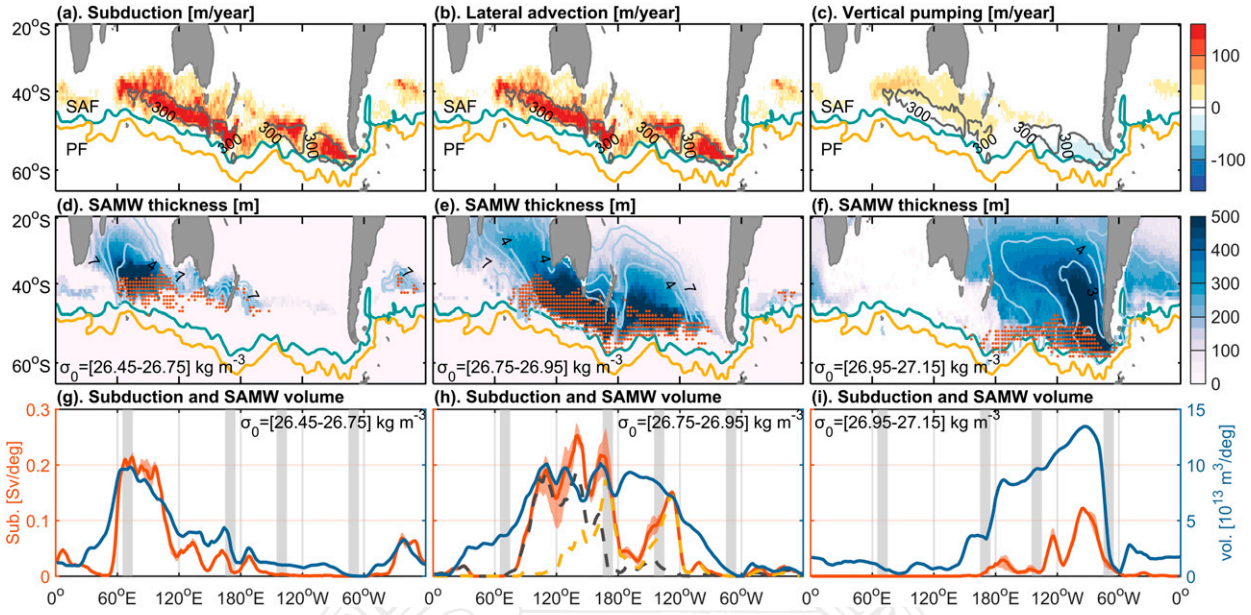

FIG. 4. Horizontal distribution of the (a) annual mean subduction rate, (b) lateral advection, and (c) vertical pumping of SAMW using the constraints described in section 3a and Table 1, calculated using Eq. (4) (all in m yr^{-1}). Dark gray lines represent the 300-m MLD in September. Blue and yellow contours as Fig. 1a. (d)–(f) Distribution of the SAMW thickness (m; blue shading) in September within σ_0 = [26.45–26.75], [26.75–26.95], and [26.95–27.15] kg m^{-3} in (d)–(f), respectively. Light blue contours represent the interior PV structure on the isopycnal surfaces. Red dots indicate grid points where both subduction takes place and the winter mixed layer is deeper than 200 m. (g)–(i) Annual subduction rate (red solid line; Sv per degree longitude) and annual mean volume of SAMW (blue solid line; $\times 10^{13}$ m^3 per degree longitude) as a function of longitude (°E) meridionally integrated south of 30°S within σ_0 range as in (d)–(f). Thick dashed black and yellow lines in (h) represent the annual subduction rate within σ_0 = [26.75–26.85] and [26.85–26.95] kg m^{-3}, respectively. The subduction rate here is the average of subduction rates estimated using three reference velocity fields described in section 2 and appendix B. Red shadings indicate uncertainties from the choice of different reference velocities compared to the average in each longitude. Gray shadings represent the location of large bathymetry: the Kerguelen Plateau (70°E), the Campbell Plateau (170°E), the Eltanin Fracture Zone (140°W), and Drake Passage (70°W), taken from Sallée et al. (2010a).

advection could play an essential role in transporting mixed layer water into the ocean interior through a shoaling mixed layer region (red shading in Fig. 3a; Fig. 2). In regions to the south of New Zealand and to the west of the Drake Passage, the ACC is squeezed into a flow with both northward and eastward shoaling mixed layers (red shading and gray dots in Fig. 3a), resulting in strong subduction (as also noted by Sallée et al. 2010a; Liu and Huang 2012).

d. Regional SAMW subduction rate at hotspots

To investigate the regional variability of SAMW and compare with subduction rates, we first consider the density distribution of SAMW volume and subduction rate estimates over the circumpolar Southern Ocean (Figs. A1g and 5b). The results show that 1) strong subduction occurs within a wide density range of σ_0 = [26.45–26.75] kg m^{-3} in the central Indian Ocean (60°–100°E, Figs. 5b,c), corresponding to the light south Indian SAMW density class and its subduction; 2) the strongest subduction in the southeast Indian Ocean (100°–165°E) occurs within σ_0 = [26.75–26.85] kg m^{-3} (Figs. 5b,d), corresponding to the southeast Indian SAMW; 3) the strongest subduction from east of Tasmania to central Pacific (165°E–120°W) occurs within σ_0 = [26.85–26.95] kg m^{-3} (Figs. 5b,e), corresponding to the central Pacific SAMW; and 4) the dominant subduction in the southeast Pacific (120°–70°W) occurs mostly within σ_0 = [26.95–27.15] kg m^{-3} (Figs. 5b,f), corresponding to the southeast Pacific SAMW. These density ranges agree well with those determined by Sallée et al. (2010a), HBR11, and Cerovečki et al. (2013) (see Figs. A1e,f and 5). The longitude and density ranges used for summing the regional subduction rate at hotspots are indicated by the red boxes in Fig. 5b; and regional SAMW types correspond to the dominant subduction at hotspots (shown in Figs. 4d–i).

Light south Indian SAMW is mainly found from the central Indian to southwest of Australia north of the Subantarctic Front (Fig. 4d), corresponding to the Indian Ocean SAMW on the 26.8-γ^n surface in HBR11 and Kolodziejczyk et al. (2019). We find there is strong subduction of 7.9 Sv dominated by lateral advection (5.9 Sv) (as also seen in Karstensen and Quadfasel 2002a,b; Sallée et al. 2010a; Liu and Huang. 2012; Portela et al. 2020) for light south Indian SAMW within the longitude band of 60°–100°E. Based on the interior PV structure (light blue contours in Fig. 4d), light south Indian SAMW can be traced from 45°S between 60° and 100°E northwestward to 20°S, east of Madagascar Island (HBR11). The volume transport of light south Indian SAMW across 30°S is estimated to be 4.2 Sv. Here the volume transport across a vertical section is calculated as $\int\int v\, dA$, where v is the meridional

JOBNAME: JPO 00#00 2021 PAGE: 8 SESS: 8 OUTPUT: Tue Aug 24 08:17:09 2021 Total No. of Pages: 22
/ams/jpo/0/jpoD200174

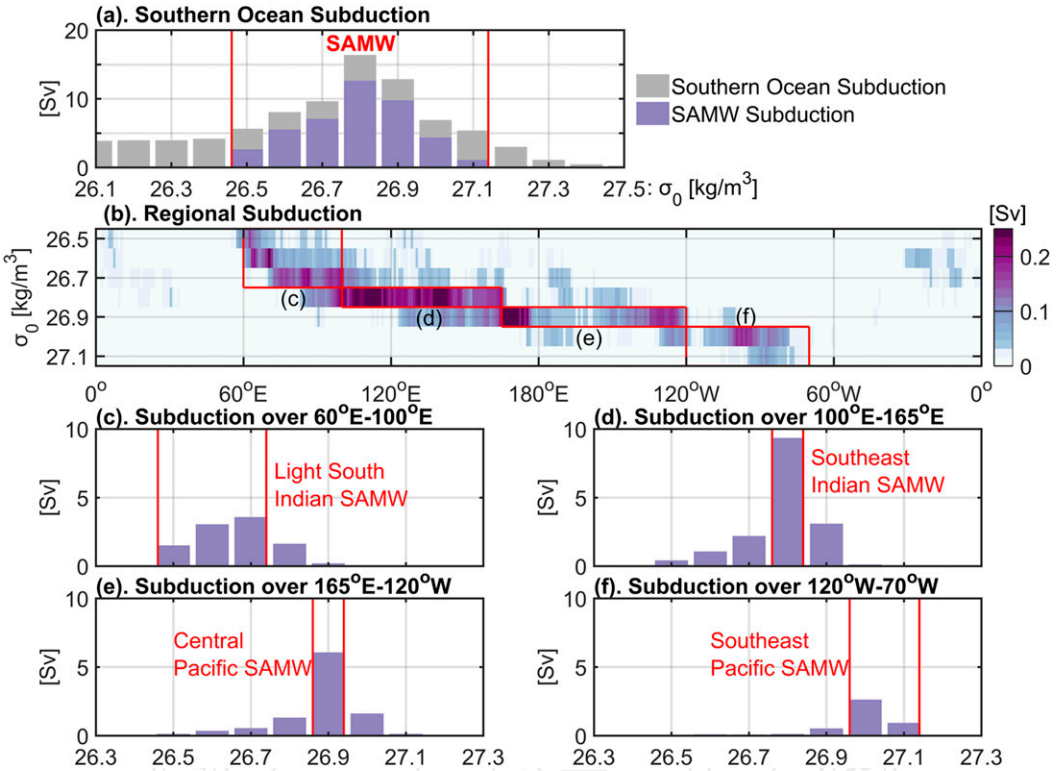

FIG. 5. (a) Annual mean subduction rate (Sv) integrated over the Southern Ocean. The annual mean subduction is partitioned into 0.1 kg m^{-3} wide density bins. Gray bars represent the annual mean subduction over the Southern Ocean and are further constrained into purple bars by adding the SAMW criteria into the calculation (section 3a). Red vertical lines indicate the lightest (densest) density surface of south Indian (southeast Pacific) SAMW subduction. (b) The annual mean subduction rate (Sv) of SAMW as a function of density and longitude, meridionally integrated south of 30°S. (c)–(f) Annual mean subduction rate (Sv) of SAMW integrated over the longitude range of 60°–100°E in (c), 100°–165°E in (d), 165°E–120°W in (e), and 120°–70°W in (f) and south of 30°S. The density classes bounded by red vertical lines in (c)–(f) indicate the dominant density layer for each SAMW type (section 4d). The longitude range and dominant density layers in (c)–(f) correspond with the red boxes in (b). The corresponding neutral density classes for the dominant potential density classes in (c)–(f) are around γ^n = [26.55–26.85], [26.85–26.95], [26.95–27.05], and [27.05–27.25] kg m^{-3}, respectively (see Figs. A1e,f).

velocity and dA is the area of the vertical section. Here v is provided as the average of geostrophic velocities derived from the no-motion choice as well as the observational based reference velocity fields (section 2). Only the volume transport of the water mass defined as SAMW is considered.

The southeast Indian SAMW and central Pacific SAMW occupy a wide region from south of Australia to the central Pacific (Fig. 4e). The southeast Indian SAMW, within the density range σ_0 = [26.75–26.85] kg m^{-3} and west of 165°E, constitutes the largest volumetric class of Indian Ocean SAMW (Fig. A1a). Its subduction rate between 100° and 165°E (black dashed line in Fig. 4h) is estimated to be 9.3 Sv, with 8.1 Sv due to lateral advection. Subsequent to subduction, this SAMW flows northwestward along the western Australian coast into the south Indian subtropical gyre (Fig. 4e), with 4.4 Sv of meridional SAMW transport at 30°S. The minimum PV value can still be found at 20°S, between 60° and 120°E, similar to SAMW on the 26.9-γ^n and 26.94-γ^n surfaces in HBR11. The central Pacific SAMW within the density range σ_0 = [26.85–26.95] kg m^{-3} mainly resides from around New Zealand to 120°W in the central Pacific, similar to the location of SAMW on the 27.0-γ^n and 27.05-γ^n surfaces in HBR11. The corresponding subduction rate (6.0 Sv between 165°E and 120°W, yellow dashed line in Fig. 4h) has two peaks, one near Campbell Plateau (170°E) and the other near the Eltanin Fracture Zone (140°W), also dominated by lateral advection (5.6 Sv) (Sallée et al. 2010a; Liu and Huang. 2012; Portela et al. 2020). The interior PV structure (Fig. 4e) suggests the PV minimum signal extends into the subtropical gyre but is restricted to the south of 30°S (only 0.8 Sv of meridional SAMW transport at 30°S) (Sallée et al. 2010a; HBR11).

The southeast Pacific SAMW spreads northward from the southeast Pacific near 55°S between 120° and 70°W (Fig. 4f) to approximately 30°S (3.4 Sv of meridional volume transport) before it turns westward, exhibiting similar patterns to SAMW on the 27.1-γ^n and 27.15-γ^n surfaces in HBR11. The Lagrangian subduction rate for this SAMW hotspot is estimated to be 3.5 Sv. Subduction in this density class can also be

JOBNAME: JPO 00#00 2021 PAGE: 9 SESS: 8 OUTPUT: Tue Aug 24 08:17:09 2021 Total No. of Pages: 22
/ams/jpo/0/jpoD200174

found west of the PV minimum core near 180°, which would suggest the southeast Pacific variety of SAMW could be partly supplied by the subducted mode water from upstream of the ACC (as seen in the Lagrangian trajectories in Fig. 3b). Subsequent to subduction, part of the southeast Pacific SAMW will reach the east coast of Australia and circulate around the Australian coast (Ridgway and Dunn 2007; Bostock et al. 2013).

Note the regional subduction estimate at each hotspot is constrained to the red boxes shown in Fig. 5b, i.e., is limited to narrow density ranges that vary with longitude, while the total SAMW subduction is integrated over the full SAMW density range and the circumpolar Southern Ocean in Fig. 5b. Therefore, the integral of regional subduction at these four hotspots does not equal the total SAMW subduction (27 versus 42 Sv). The location of SAMW subduction hotspots and export pathways are consistent with previous studies (e.g., Sallée et al. 2010a; Koch-Larrouy et al. 2010; HBR11; Cerovečki et al. 2013; Jones et al. 2016). In all four subduction hotspots, a positive gradient of MLD in the northeast direction (Fig. 3a) provides the ideal environment for lateral advection to take place [i.e., with $\nabla h > 0$ in Eq. (1)]. The regions of strong subduction are characterized by a minimum in PV, since the ocean interior is spiked with low PV mixed layer water by the subduction process. Due to the intrusion of large volumes of mode water from the upper layer, the distance between isopycnal surfaces is expanded. This increases the thickness and volume of SAMW at longitudes with large subduction rates, in agreement with Sallée et al. (2010a) and HBR11. Finally, PV minimum layers in each density class are exported away into the subtropical gyres through these exchange windows.

e. Subduction in Lagrangian and Eulerian coordinates

SAMW formation by annual mean subduction is given as 42 ± 7 Sv from the Lagrangian approach [Eq. (4)] during the analysis period 2004–18. In comparison, the Eulerian subduction approach in Eq. (1) gives about 12 Sv of annual net mass flux across the base of the maximum mixed layer. This is because the Lagrangian subduction represents only the annual net effective detrainment across the base of the mixed layer, while in the Eulerian coordinates, subduction is defined as the annual net mass flux at each station of the maximum mixed layer base. The entrainment rate excluded from the Lagrangian approach but included in the Eulerian subduction calculation could thus induce different values of the SAMW subduction estimate. Moreover, the Lagrangian method measures subduction from a nonlocal viewpoint of the MLD movement between adjacent years, which makes it hard to define the net mass flux across each station of the winter mixed layer base. Therefore, the Lagrangian subduction is mainly applied to understand the spatial and interannual variability in the annual SAMW formation by subduction in this study. For instance, by comparing with the annually averaged volume formation derived from a volumetric method [Eqs. (C1) and (C2), appendix C] (Davis et al. 2011), contributions from the annual mean subduction rate to the annual volume formation of the interior SAMW can be about a half (Fig. C2b), suggesting the vital role of subduction in SAMW formation. As for the comparison with the monthly SAMW formation by air–sea fluxes and monthly SAMW volume change, the subduction estimate in Eulerian coordinates is applied in sections 6 and 7 and appendix C.

5. Thermodynamic estimate of surface water-mass transformation

Water-mass transformation (WMT) is the exchange of volume between water masses with different properties, such as salinity, temperature, or buoyancy. The surface water-mass transformation rate F and formation rate ΔF, driven by the air–sea buoyancy fluxes, are estimated here following the approach of Maze et al. (2009) and Cerovečki et al. (2013) [Eqs. (D1)–(D3), appendix D].

A positive WMT rate mainly appears during April–September (Fig. 6a) when the ocean surface loses buoyancy. The convergence of WMT rate results in a positive formation rate within the SAMW density range ($\Delta F > 0$), especially for densities between 26.75 and 27.05 kg m^{-3} (Fig. 6c). This supports the formation of deep wintertime mixed layers and thus the formation of SAMW. The two peaks in water-mass formation rates at σ_0 = 26.8 and 27.0–27.05 kg m^{-3} correspond to SAMW peaks in the Indian and Pacific Oceans (Fig. A1a), respectively (HBR11; Cerovečki et al. 2013). For the months of October–March, the negative surface water-mass formation is found at the density outcrops of σ_0 = 26.8 kg m^{-3} (Fig. 6d). In this study, SAMW formation by air–sea buoyancy fluxes is integrated within a fixed density range of σ_0 = [26.5–27.1] kg m^{-3} over the Southern Ocean, which gives an annual mean value of ~31 ± 7 Sv.

6. Seasonal SAMW volume variability

In the above, we discussed the mean SAMW formation over the period 2004–18 due to the subduction process and air–sea buoyancy fluxes. Previous studies have shown the important roles of subduction and air–sea buoyancy fluxes in the seasonal cycle of SAMW formation (Kwon 2013; Kwon et al. 2013; Evans et al. 2014, 2018; Cerovečki and Mazloff 2016). Here, we calculate the month-to-month variation of these processes, and compare SAMW volume changes with SAMW formation due to air–sea fluxes [Eqs. (D1) and (D2)] and monthly subduction rates [Eq. (1)]. Importantly, we separately consider SAMW formation processes within the monthly mixed layer ($SAMW_{ML}$) and in the interior below the mixed layer ($SAMW_{INT}$) to compare their evolution in time. We find that the formation of $SAMW_{ML}$ is dominated by air–sea formation, whereas most of the $SAMW_{INT}$ is formed from subducted $SAMW_{ML}$ during a limited period of the year when the mixed layer and the ocean interior are connected by deep winter mixed layers. Here we will refer to this connection as the ''low PV bridge,'' as described later.

SAMW volume peaks in September and reaches a minimum in May (Fig. 7a), with an annual amplitude of 3.6×10^{15} m^3. From December to March, almost 100% of the total SAMW volume is below the mixed layer ($SAMW_{INT}$, Fig. 7g), while between April and November up to 10% of the SAMW volume

JOBNAME: JPO 00#00 2021 PAGE: 10 SESS: 8 OUTPUT: Tue Aug 24 08:17:09 2021 Total No. of Pages: 22
/ams/jpo/0/jpoD200174

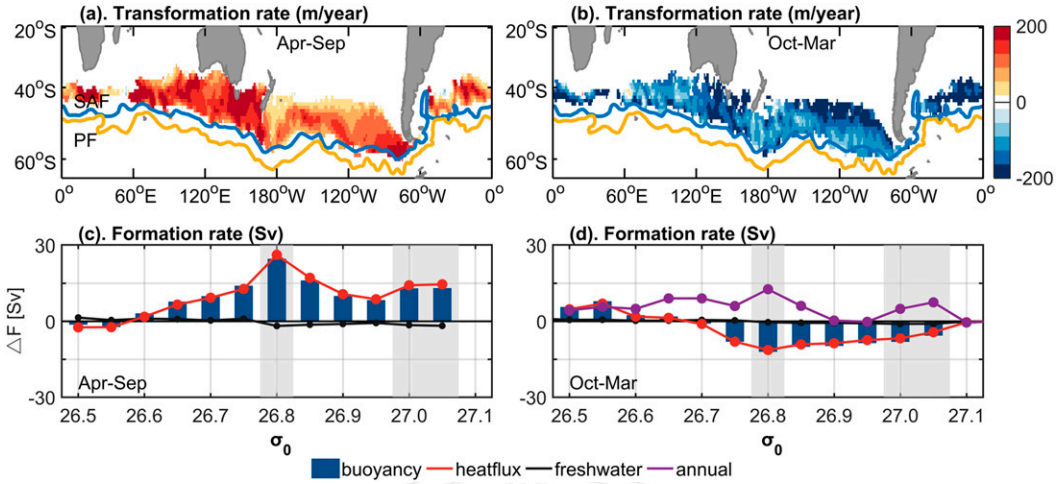

FIG. 6. Horizontal distribution of transformation rate (Sv) due to surface buoyancy fluxes averaged over the (a) buoyancy loss season (April–September) and (b) buoyancy gain season (October–March), respectively. A positive transformation rate corresponds to conversion of light water into denser water across a given isopycnal σ_0. Blue and yellow contours are as in Fig. 1a. The Southern Ocean (south of 30°S) averaged water-mass formation rates during the (c) buoyancy loss and (d) buoyancy gain seasons. All estimates have been binned into 0.05 kg m^{-3} density bins. Blue bars indicate the formation rate from the surface buoyancy flux. Red and black lines represent contributions from the surface heat flux and freshwater flux, respectively. The purple line in (d) shows the annual mean formation rate due to air–sea interaction, which is the sum of formation rates shown in (c) and (d). Gray shading indicates two peaks in the surface formation by buoyancy flux in the Southern Ocean, corresponding to the southeast Indian SAMW (with a core density $\sigma_0 = 26.8$ kg m^{-3}) and southeast Pacific SAMW (with a core density around 27.0–27.05 kg m^{-3}).

is in the mixed layer ($SAMW_{ML}$, Fig. 7d). The seasonal variability of $SAMW_{ML}$ volume is about 1.5 times larger than that of $SAMW_{INT}$ (i.e., amplitude of 5.0×10^{15} versus 2.9×10^{15} m^3), with two months offset between their respective peaks (September versus November, Figs. 7d,g). Hence, even though $SAMW_{ML}$ volume is less than a tenth of the total volume, it dominates the seasonal variability in the SAMW volume budget.

We next consider estimates of SAMW formation using monthly variations of the volume anomalies (Figs. 7b,e,h, as in Fig. 8c of Kwon 2013). In particular, this is derived as $\partial V/\partial t = (V_{n+1} - V_n)/\Delta t$, where V_n is the volume of SAMW at month n, and Δt is a one-month time increment. The SAMW criteria of Table 1 are imposed for the estimate of SAMW volume and SAMW formation by instantaneous subduction [Fig. 7i, Eq. (1)] and air–sea buoyancy fluxes (section 3a). The Ekman transport across the Subantarctic Front is roughly estimated by $M_y = -\tau_x/(\rho_0 f)$. These estimates are summarized in Fig. 8 to show the annual cycle of SAMW. The percentage provided below indicates the SAMW formation estimate divided by SAMW volume change shown in Fig. 8.

Positive volume changes of $SAMW_{ML}$ occur from January to August and negative volume change is apparent from September to December (Fig. 7e) (as in Fig. 8c of Kwon 2013). The timing of $SAMW_{ML}$ volume increase corresponds closely to SAMW formation by surface buoyancy fluxes (Figs. 7c,e). The air–sea interaction induced WMT contributes to the formation and destruction of the mixed layer water and therefore, the $SAMW_{ML}$ volume changes (Figs. 7c,f,e). For the surface buoyancy loss period of April–August (Figs. 8a,b), air–sea formation can explain about 40% of the volume increase in $SAMW_{ML}$. In the late winter months July–August (Fig. 8b), an average formation rate of 180 Sv by surface buoyancy fluxes can explain about 45% of the 400 Sv volume increase rate in $SAMW_{ML}$. At the same period (Fig. 8b), about 35% of the volume increase in $SAMW_{ML}$ can be accounted for by entrainment (−140 Sv, Fig. 7i), while about 10% may originate from the northward Ekman transport across the Subantarctic Front (41 Sv). The remaining 10% of the $SAMW_{ML}$ volume increase must be balanced by contributions from WMT by diapycnal mixing (Iudicone et al. 2008, 2011; Cerovečki and Mazloff 2016; Portela et al. 2020), and perhaps by cabbeling and thermobaricity (Groeskamp et al. 2016).

The monthly volume change of $SAMW_{ML}$ (Fig. 7e) is almost out of phase with the monthly subduction (Fig. 7i) (Kwon 2013), while the monthly $SAMW_{INT}$ volume change (Fig. 7h) and subduction share similar seasonal signals. This indicates that the detrainment and entrainment of water across the mixed layer base are essential for water exchange between $SAMW_{ML}$ and $SAMW_{INT}$, as explained below. Both MLD and $SAMW_{ML}$ volume reach their maximum value around September, then start to decrease (Figs. 7d,f and 8c,d). The mixed layer shallows largely due to restratification by surface buoyancy gain (Fig. 7c). However, only a small portion of $SAMW_{ML}$ (4% during September–October, Fig. 8c) near the surface is destroyed by air–sea interaction, while most remains in the subsurface due to the shoaling mixed layer, which will potentially subduct to form $SAMW_{INT}$. During

JOBNAME: JPO 00#00 2021 PAGE: 11 SESS: 8 OUTPUT: Tue Aug 24 08:17:09 2021 Total No. of Pages: 22
/ams/jpo/0/jpoD200174

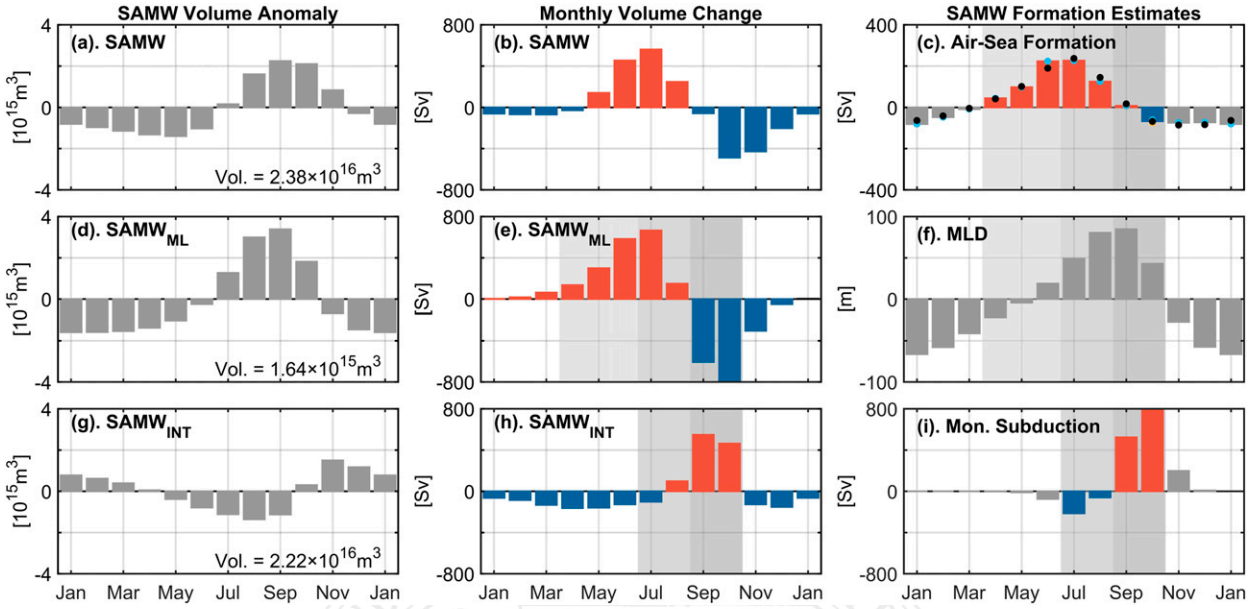

FIG. 7. Monthly volume anomalies (10^{15} m^3) of the (a) total SAMW, (d) SAMW$_{ML}$, and (g) SAMW$_{INT}$. The average volume of SAMW over the analysis period is provided on the bottom right of each panel. Middle column is the monthly volume change rate (Sv) of (b) total SAMW, (e) SAMW$_{ML}$, and (h) SAMW$_{INT}$ estimated as $\partial V/\partial t = (V_{n+1} - V_n)/\Delta t$. Positive values [red bars in (b), (e), and (h)] represent an increase and negative values (blue bars) a decrease of SAMW volume. (c) Net surface formation rate (Sv) integrated within zonally fixed density ranges of σ_0 = [26.5–27.1] kg m^{-3} (bars), σ_0 = [26.6–27.0] kg m^{-3} (black dots), σ_0 = [26.5–27.0] kg m^{-3} (blue dots), and σ_0 = [26.6–27.1] kg m^{-3} (yellow dots), diagnosed from Eq. (D2) (see appendix D). (f) Anomaly of the monthly MLD averaged over the SAMW outcrop windows. (i) Monthly subduction rate in the SAMW density range (Sv) based on Eq. (1). Positive values in (i) indicate detrainment from the mixed layer into ocean interior and negative values represent entrainment.

September–October, large values of the volume change in SAMW$_{ML}$ and SAMW$_{INT}$ can be found with an opposite sign (Figs. 7e,h). About 85% of the volume decrease in SAMW$_{ML}$ can be explained by subduction, by comparing the SAMW$_{ML}$ volume change (Fig. 7e) with the monthly subduction rate (Fig. 7i) during September–October (Fig. 8c). This amount of mode water subducted from SAMW$_{ML}$ can explain virtually all of the volume increase of SAMW$_{INT}$ over the same period (Figs. 7h and 8c). From November onward, both SAMW$_{ML}$ volume and SAMW$_{INT}$ volume decrease (Figs. 7e,h and 8d) due to surface buoyancy gain (Fig. 7c), meridional transport of SAMW leaving the Southern Ocean, and mixing processes in the mixed layer and the interior ocean (e.g., Sloyan and Rintoul 2001; Iudicone et al. 2008, 2011; Evans et al. 2014; Groeskamp et al. 2017; Portela et al. 2020).

To evaluate the seasonal evolution of the low PV signal from the mixed layer to the ocean interior, we consider the monthly PV and MLD averaged over the Indian and Pacific Oceans (Fig. 9). Here the monthly mean PV averaged vertically between the base of the monthly mixed layer and the maximum mixed layer (red-brown lines in Figs. 9a,b) indicates the strength of the mean stratification between the mixed layer and the ocean interior. PV at the maximum mixed layer base (blue lines in Figs. 9a,b) represents the stratification at the top of the ocean interior. From November to July, there is a stratified layer between the mixed layer and the interior (Fig. 9). This strong stratification obstructs the exchange between the mixed layer and the pycnocline. However, during July–August, the seasonal stratified layer gets destroyed and the exchange of mode water begins. The monthly subduction then takes place from August to October (Figs. 7h,i and 9c,d), when the mixed layer is deepest and then starts to shallow. During this period, SAMW$_{ML}$ and SAMW$_{INT}$ are connected by a low PV bridge. That is, the low PV from the surface to intermediate depth allows for a rapid exchange between the mixed layer and the ocean interior. This causes a decrease of SAMW$_{ML}$ volume and an increase of SAMW$_{INT}$ volume (Figs. 7e,h and 8c).

The instantaneous subduction at the monthly mixed layer base occurs mainly during August–October, depending on the condition of the low PV bridge (Fig. 9). However, the mass flux across the base of the maximum mixed layer, which is used to define the annual mass flux into the permanent pycnocline (Williams 1991; Marshall et al. 1993, 1999), could last longer due to the remaining mode water above the maximum mixed layer base (Figs. 9c,d, compare blue solid lines with gray dashed lines in Figs. 9a,b). From the PV value at the base of the maximum mixed layer, the time period of the SAMW injection could be defined at each station. It would suggest that combining the subduction process with the low PV bridge would have implications for defining the local annual net mass flux of SAMW into the permanent pycnocline, similar to the effective subduction period defined in Marshall et al. (1993) but from a

JOBNAME: JPO 00#00 2021 PAGE: 12 SESS: 8 OUTPUT: Tue Aug 24 08:17:10 2021 Total No. of Pages: 22
/ams/jpo/0/jpoD200174

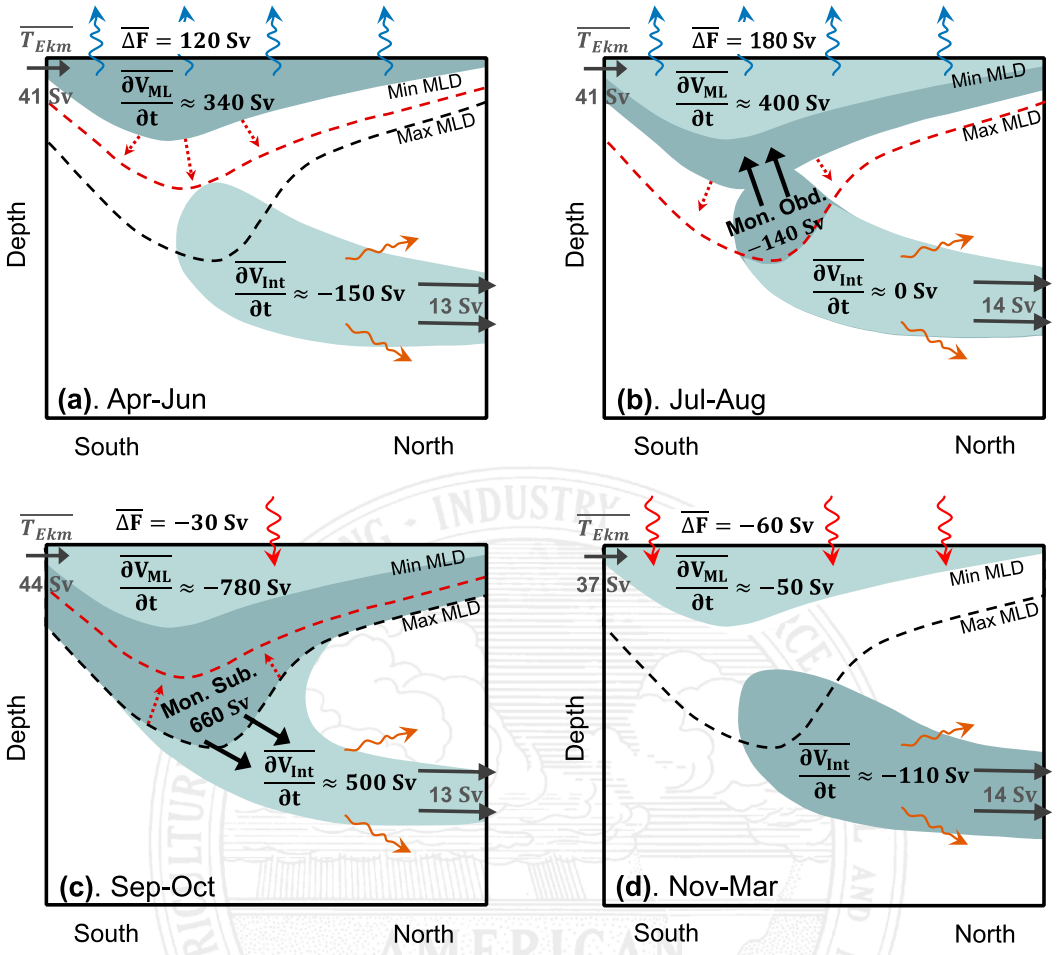

FIG. 8. Schematic of the formation and destruction of SAMW over the course of a year. (a) Onset of the deepening of mixed layers (April–June). (b) Obduction occurs when mixed layers deepen and reentrain mode water into the mixed layer (July–August). (c) Subduction takes place when the MLD is deepest (September–October). (d) MLD returns to its minimum when the restratification occurs in late spring (November–March). Here, ΔF represents the water-mass formation rate induced by air–sea buoyancy fluxes [Eq. (D2)], T_{Ekm} denotes the northward Ekman transport across the Subantarctic Front. V_{ML} and V_{Int} are the volume of $\mathrm{SAMW_{ML}}$ and $\mathrm{SAMW_{INT}}$, respectively. Dark gray arrows across the right boundary of each panel indicate the meridional volume transport of SAMW at 30°S. Note the values provided in each panel are the average over different panels.

viewpoint of PV limits at the upper surface of the permanent pycnocline.

7. The role of ocean mixing

So far we focused on the volume budget of SAMW in the mixed layer and below, combined with an estimate of the air–sea formation and subduction. However, mixing has been suggested to be a significant contributor to the volume variability of SAMW (Sloyan and Rintoul 2001; Evans et al. 2014, 2018; Cerovečki and Mazloff 2016; Portela et al. 2020). Here we will provide a rough indication of the effect of mixing on the SAMW volume budget using the WMT framework in Groeskamp et al. (2019a,b). This, however, requires us to deviate from the previous definition of SAMW and define SAMW as all waters within the neutral density range $\gamma^n = [26.55\text{–}27.25]\ \mathrm{kg\,m^{-3}}$ (hereafter referred to as the "SAMW layer" to differentiate this layer from the SAMW definition used in previous sections).

The estimate of SAMW formation due to mixing depends strongly on the choice for eddy diffusivities in space and time (Groeskamp et al. 2016, 2017, 2020; de Lavergne et al. 2020). To obtain an estimate of the SAMW formation due to isopycnal mixing (i.e., cabbeling and thermobaricity) and diapycnal mixing (i.e., vertical mixing), we will simply assume a constant mesoscale eddy diffusion coefficient of $K = 500\ \mathrm{m^2\,s^{-1}}$ and a constant vertical diffusion coefficient of $D = 3 \times 10^{-5}\ \mathrm{m^2\,s^{-1}}$. This provides formation rates within the neutral density range $\gamma^n = [26.55\text{–}27.25]\ \mathrm{kg\,m^{-3}}$ ranging between −25 and 5 Sv in the annual cycle, with a mean value of about −13 Sv, which agree with previous estimates (Downes et al. 2011xx; Iudicone et al. 2008). AU5

JOBNAME: JPO 00#00 2021 PAGE: 13 SESS: 8 OUTPUT: Tue Aug 24 08:17:10 2021 Total No. of Pages: 22
/ams/jpo/0/jpoD200174

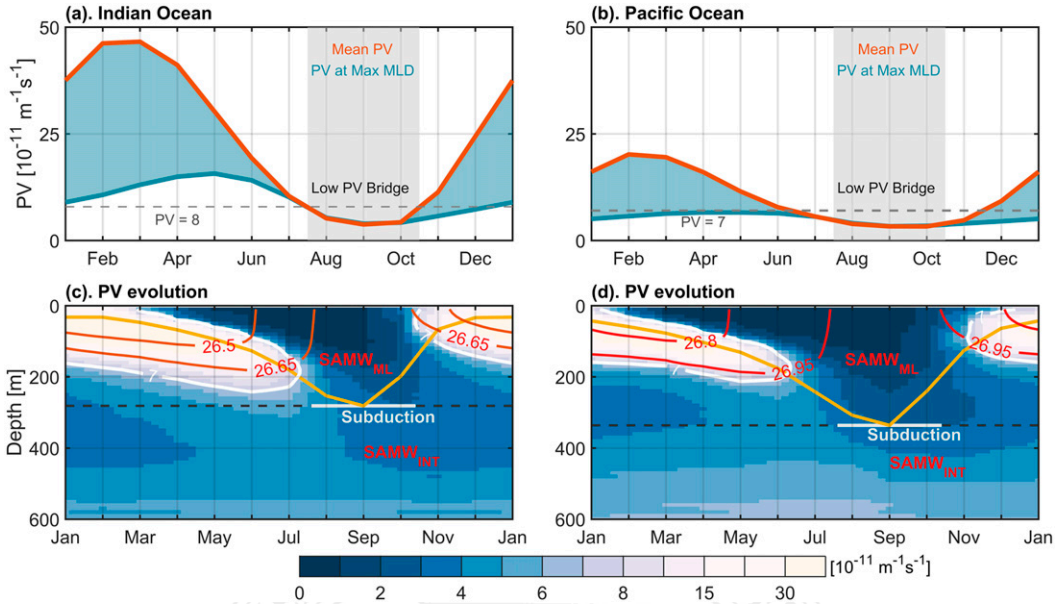

FIG. 9. Climatological monthly PV ($\times 10^{-11}$ m^{-1} s^{-1}) at the maximum MLD (blue line) and mean PV between the monthly mean MLD and maximum MLD (red-brown line), averaged over (a) 60°–160°E and (b) 140°–70°W, all south of 30°S. Gray shadings represent August–October, which is the effective detrainment period (i.e., subduction) in the Southern Ocean. Horizontal gray dashed lines indicate the PV value of 8×10^{-11} and 7×10^{-11} m^{-1} s^{-1}, respectively. Also shown are the seasonal evolution of PV (shadings and thick white lines), MLD (yellow lines), and isopycnals (red lines), averaged over (c) 60°–160°E and (d) 140°–70°W, all south of 30°S. Only areas with deep winter mixed layers (MLD > 150 m in the Indian, and MLD > 200 m in the Pacific) are considered.

We further separate the WMT by ocean mixing in "source" regions (i.e., within the maximum mixed layer) from the WMT by ocean mixing in "sink" regions (i.e., the ocean interior) to see the balance of mixed layer mixing against surface forcing and subduction in source regions, and the balance of interior mixing against subduction and volume fluxes out of the domain in sink regions, respectively. The resulting ocean mixing within the maximum mixed layer and within the ocean interior south of 30°S are estimated as about −4 and −8 Sv in the annual mean, respectively.

We next combine subduction with water-mass formation due to air–sea buoyancy fluxes and ocean mixing (all for the neutral density range γ^n = [26.55–27.25] kg m^{-3}). The net formation by air–sea buoyancy fluxes over the SAMW layer in the Southern Ocean is estimated at ~21 Sv and can only be balanced in the steady state by diapycnal volume transport to other densities (~13 Sv), or via export out of the Southern Ocean. In this regard, our results suggest that ~4 Sv of the ~21 Sv air–sea formation mixes away within the maximum mixed layers, while the rest of the waters subduct into the ocean interior by Ekman pumping and lateral advection (~12 Sv), and also by eddy-induced subduction (~6 Sv; from Lee et al. 2011). The subducted volume includes both waters that move north from the ACC into the subtropical gyres and waters that reentrain back into the ACC. Of the water that is subducted over the SAMW layer, a certain portion can be mixed away by the interior ocean mixing (~8 Sv), and part of this mixing could supply the AAIW layer via diapycnal exchange (e.g., Iudicone et al. 2008; Downes et al. 2011xx; AU6 Evans et al. 2014; Portela et al. 2020).

The use of the constant K and D fields in estimating the ocean mixing may cause uncertainties in the above WMT analysis. In this study, however, we focus on the roles of Lagrangian subduction in setting SAMW formation hotspots, Eulerian subduction in the exchange between $SAMW_{ML}$ and $SAMW_{INT}$, and air–sea formation in driving vigorous mixed layer convection in winter. A much more detailed calculation and analysis of WMT by mixing will follow in our future work.

8. Conclusions

In this study we used observationally based Argo data to quantify, compare, and contrast mechanisms of SAMW formation over the seasonal cycle and for the annual mean state. We further considered the mixed layer SAMW changes and the interior SAMW changes separately, to be able to individually examine the dynamics related to their formation, and subsequently study the exchange between these two components.

First, we quantified the annual mean subduction at so-called SAMW subduction hotspots from a Lagrangian approach that provides the annual mean subduction rate of SAMW, while also revealing the 1-yr trajectory of each subducted SAMW parcel. Our results of subduction hotspots and export pathways of SAMW are consisted with those of Herraiz-Borreguero and Rintoul (2011) and Kolodziejczyk et al. (2019).

JOBNAME: JPO 00#00 2021 PAGE: 14 SESS: 8 OUTPUT: Tue Aug 24 08:17:10 2021 Total No. of Pages: 22
/ams/jpo/0/jpoD200174

We find that in the south Indian Ocean, strong SAMW subduction occurs in two locations, one lying north of 45°S between 60° and 100°E and the other appearing south of Australia between 100° and 165°E. These two hotspots produce about 8 and 9 Sv of SAMW subduction for the light and southeast Indian SAMW, respectively. In the South Pacific Ocean, strong SAMW subduction of ~6 Sv occurs east of New Zealand to 120°W for the central Pacific SAMW, as well as a subduction of ~4 Sv between 120° and 70°W for the southeast Pacific SAMW.

Second, our results suggest the following mechanism for the seasonal cycle of SAMW formation and destruction, summarized by the schematic shown in Fig. 8. From autumn to winter (April–August), surface buoyancy loss on the equatorward side of the Subantarctic Front leads to a deepening of winter mixed layers and the formation of $SAMW_{ML}$ (Fig. 8a–c). Both the MLD and $SAMW_{ML}$ volume reach maximum value around August–September (Fig. 8c), during which time the mixed layer and ocean interior are connected by the deep winter mixed layer. The deep winter mixed layer carries low PV values, thereby opening up for exchange with the interior. We refer here to this as the low PV bridge. At this time, mode water subducts into the interior to form $SAMW_{INT}$ (Figs. 9c,d). The exchange of SAMW volume between the mixed layer ($SAMW_{ML}$) and the interior ($SAMW_{INT}$) is measured by the instantaneous subduction rate [Eq. (1)] and the annual mean subduction rate [Eq. (4)]. The mixed layer to interior exchange is also partly due to diapycnal mixing (Portela et al. 2020) and heaving (Kolodziejczyk et al. 2019). The focus of this study, however, is to measure the subduction in the annual cycle of the exchange between $SAMW_{ML}$ and $SAMW_{INT}$.

In spring and summer (October–March), when the ocean surface gains buoyancy, outcropping isopycnals flatten and the mixed layer shoals (Figs. 9c,d and 8d). Consequently, a portion of the $SAMW_{ML}$ gets destroyed by restratification of the surface layer, while most of the $SAMW_{ML}$ remains in the subsurface because of the shoaling mixed layer. The remaining mode water would probably become $SAMW_{INT}$ or mix with its surrounding water into a different water mass (Figs. 9c,d and 8d). The volume of $SAMW_{INT}$ reaches its maximum around November (Fig. 7g). As the surface stratification strengthens and deepens, the low PV bridge breaks and any exchange between the mixed layer and the interior finally stops (Fig. 9). After November, the $SAMW_{INT}$ volume steadily decreases (Figs. 7h and 8d), probably due to mixing processes and the meridional transport of $SAMW_{INT}$ leaving the Southern Ocean (~13 Sv of meridional SAMW transport at 30°S).

This study has provided new insights into understanding the seasonal evolution of SAMW by treating SAMW as a combination of its components within the mixed layer and in the ocean interior. Understanding the formation process of SAMW has implications for the uptake and redistribution of heat and carbon by the global ocean.

Acknowledgments. Zhi Li received support from the Foundation of China Scholarship Council (201806330075), Climate Change Research Centre (CCRC), University of New South Wales, and Centre for Southern Hemisphere Ocean Research (CSHOR), a joint research centre between QNLM, CSIRO, UNSW, and UTAS. This study was supported by the Australian Research Council (ARC Grant CE17010023). M.H.E. is also supported by the Centre for Southern Hemisphere Oceans Research (CSHOR), a joint research center between QNLM, CSIRO, UNSW, and UTAS. IC received support from National Science Foundation Award OCE-1658001 and NASA Grant 80NSSC19K1115. YYL is supported by the National Key Research and Development Program of China (2018YFA0605702) and the National Natural Science Foundation of China (41976006). We thank George Nurser and Esther Portela for their insightful comments that helped to improve this paper. The gridded RG09 Argo data product has been continuously updated at http://sio-argo.ucsd.edu/RG_Climatology.html. These data were collected and made freely available by the International Argo Program and the national programs that contribute to it (http://www.argo.ucsd.edu, http://argo.jcommops.org). The Argo Program is part of the Global Ocean Observing System. The ERA-Interim dataset, developed by the European Centre for Medium-Range Weather Forecasts, was obtained from https://www.ecmwf.int/en/forecasts/datasets/reanalysis-datasets/era-interim. The observationally based velocity fields were downloaded at http://apdrc.soest.hawaii.edu/projects/yomaha/ and http://alisonrgray.com/agva/. GSW Toolbox, http://www.teos-10.org/software.htm.

APPENDIX A

Identification of SAMW

To identify the PV limit and density range of SAMW in the main SAMW formation regions, we consider the volume of low PV water (under low PV constraints) as a function of density (Fig. A1a). Low PV water can be found in the density range of FA1 σ_0 = [26.5–27.0] kg m^{-3} in the Indian, and σ_0 = [26.6–27.1] kg m^{-3} in the Pacific Ocean, which can also be found from the volume distribution of low PV water by density and latitude in Fig. A1g. We test low PV limits from 4 to 15 × 10^{-11} m^{-1} s^{-1} and find the core of SAMW remains the same, which is σ_0 = 26.825 kg m^{-3} in the Indian, and σ_0 = 26.975 kg m^{-3} in the Pacific, corresponding to the density with minimum PV (Fig. A1b). In addition, we also calculate the mean S_A and Θ as a function of density, only sampling the SAMW density range, to provide the corresponding range of S_A and Θ in the Indian and Pacific Oceans (Figs. A1c,d).

To summarize, we identify SAMW in the Pacific as the PV minimum layer (PV < 7 × 10^{-11} m^{-1} s^{-1}) within σ_0 = [26.6–27.1] kg m^{-3}, Θ = [4–14]°C, and S_A = [34.2–35.2] g kg^{-1}, respectively. In the Indian sector, we identify SAMW as the low PV layer (PV < 8 × 10^{-11} m^{-1} s^{-1}) within σ_0 = [26.5–27.0] kg m^{-3}, Θ = [4–15]°C, and S_A = [34.4–35.6] g kg^{-1}, respectively. We use the same identification of Atlantic SAMW as in the Indian Ocean.

We also determined the neutral density ranges of SAMW by a linear regression between σ_0 and γ^n (Figs. A1e,f). It turns out that the γ^n ranges of SAMW corresponding to σ_0 are γ^n = [26.54–27.12] and [26.66–27.25] kg m^{-3} in the Indian and Pacific Oceans (Table 1), respectively.

JOBNAME: JPO 00#00 2021 PAGE: 15 SESS: 8 OUTPUT: Tue Aug 24 08:17:10 2021 Total No. of Pages: 22
/ams/jpo/0/jpoD200174

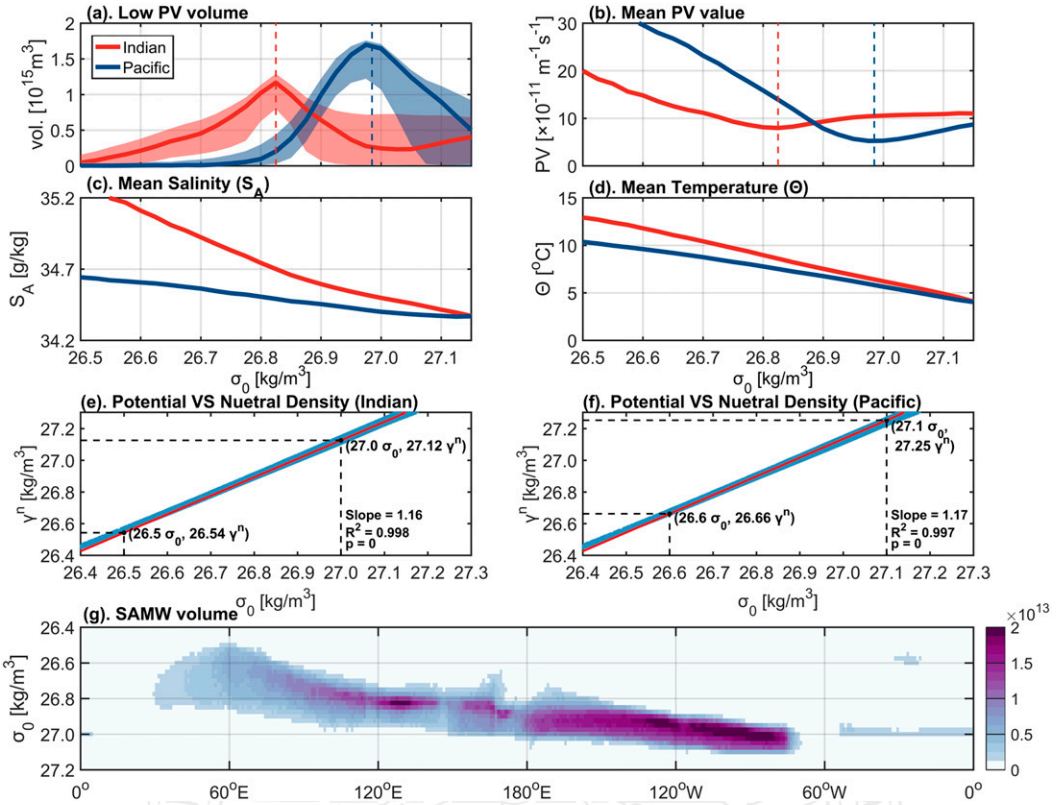

FIG. A1. (a) Density binned annual mean volume (10^{15} m^3) of water in the Indian (30°–175°E; red) and Pacific (176°E–60°W; blue) Oceans that satisfies low PV constraint in the range from 4 to 15 × 10^{-11} m^{-1} s^{-1} (shaded area), and for the low PV values used as thresholds to identify SAMWs: PV ≤ 8 × 10^{-11} m^{-1} s^{-1} in the Indian and PV ≤ 7 × 10^{-11} m^{-1} s^{-1} in the Pacific Ocean (solid lines). Density binned annual mean (b) PV (10^{-11} m^{-1} s^{-1}), (c) Absolute Salinity (g kg^{-1}), and (d) Conservative Temperature (°C) in the Indian (red solid line) and Pacific (blue solid line) Oceans. All data have been binned into 0.025 kg m^{-3} wide density bins. Linear regression of the potential density, σ_0, and neutral density γ^n in the (e) Indian (30°–175°E) and (f) Pacific (176°E–60°W) Oceans. Blue dots are water particles in the Indian and Pacific Oceans. Red solid lines indicate the linear regression of σ_0 and γ^n, with the slope of the regression line, R^2 statistic, and p value shown on the bottom right of each panel. Black dashed lines indicate the corresponding γ^n and σ_0 of the SAMW density constraints in the Indian and Pacific Oceans, respectively. (g) The volume of SAMW (×10^{13} m^3) as a function of density and longitude, integrated over the Southern Ocean. All obtained from the RG09 Argo product for 2004–18.

APPENDIX B

Uncertainties in SAMW Subduction Estimates

The MLD and geostrophic velocity influence the subduction estimates [Eqs. (1) and (4)]; here we evaluate the sensitivity of subduction to different choices of the MLD criteria and the method used to compute geostrophic velocities. We do so by repeating the calculations for different MLD estimates, and different geostrophic velocity estimates. We find the choices slightly influence the quantitative results, but not the main conclusion of this study.

a. Mixed layer depth

Various criteria have been used to calculate the MLD in past studies. Here, we examine the density-based criteria of $\Delta\sigma_0 \leq 0.03$ kg m^{-3} (de Boyer Montégut et al. 2004) and $\Delta\sigma_0 \leq 0.125$ kg m^{-3} (Monterey and Levitus 1997), as well as the temperature-based criteria of $\Delta\Theta \leq 0.2$°C (de Boyer Montégut et al. 2004) and $\Delta\Theta \leq 0.5$°C (Obata et al. 1996; Monterey and Levitus 1997). All four criteria consider the difference relative to the σ_0 or Θ at 10-m depth. The MLD estimates from these four criteria have similar patterns north of the Subantarctic Front but show large differences in magnitude (Figs. 2a and B1a–c). For FB1 instance, the MLD obtained using the density threshold of $\Delta\sigma_0 \leq 0.125$ kg m^{-3} is almost twice as deep as that obtained using $\Delta\sigma_0 \leq 0.03$ kg m^{-3} on the north flank of the ACC in both the Indian and Pacific sectors (Fig. B1a). However, we find that the $\Delta\sigma_0 \leq 0.125$ kg m^{-3} threshold is not applicable for our purpose because this criterion yields a MLD estimate that is well below the mixed layer in the Southern Ocean (refer to empty circle in Fig. B1d). We decide to use this MLD criterion to test the sensitivity of subduction because we wish to assess our calculations relative to a very different MLD

JOBNAME: JPO 00#00 2021 PAGE: 16 SESS: 8 OUTPUT: Tue Aug 24 08:17:11 2021 Total No. of Pages: 22
/ams/jpo/0/jpoD200174

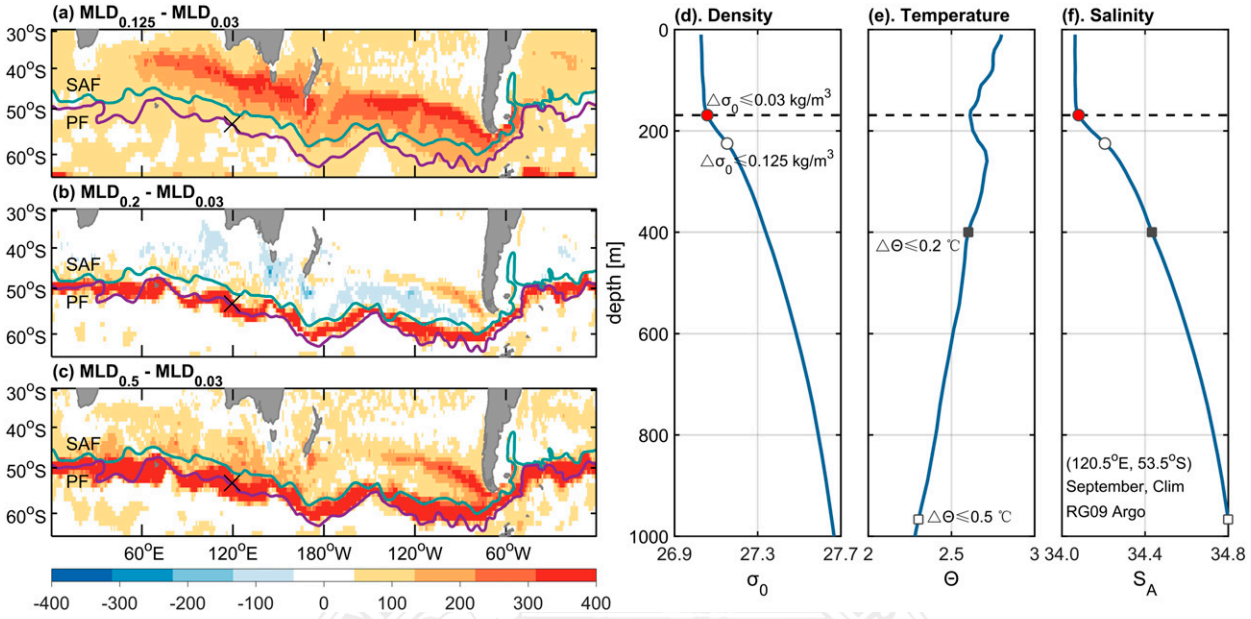

FIG. B1. Spatial distribution of the differences in September MLD using MLD criteria of (a) $\Delta\sigma_0 \leq 0.125\,\mathrm{kg\,m^{-3}}$, (b) $\Delta\Theta \leq 0.2$°C, and (c) $\Delta\Theta \leq 0.5$°C relative to the MLD calculated using the threshold of $\Delta\sigma_0 \leq 0.03\,\mathrm{kg\,m^{-3}}$ in Fig. 2a, respectively. Blue and purple contours are as in Fig. 1a. Depth profiles of (d) potential density (σ_0; $\mathrm{kg\,m^{-3}}$), (e) Conservative Temperature (Θ; °C), and (f) Absolute Salinity (S_A; $\mathrm{g\,kg^{-1}}$) at the location of 53.5°S, 120.5°E from RG09 [shown as the black cross in (a)–(c)]. The depth at which the difference in density is 0.03 or 0.125 $\mathrm{kg\,m^{-3}}$ compared to 10 m, is indicated with a solid circle or empty circle. Solid square and empty square represent the MLD using the Conservative Temperature threshold of 0.2° and 0.5°C, respectively. The black dash line indicates the MLD from the criteria of $\Delta\sigma_0 \leq 0.03\,\mathrm{kg\,m^{-3}}$.

metric to see how robust the results are. This provides a more stringent test of the robustness of our calculations compared to testing with a similar MLD criteria. The MLD criteria based on temperature are also inappropriate for our purposes because salinity plays an essential role in defining seawater density and MLD, especially near the Subantarctic Front and northwest of the Drake Passage (Fig. B1). Therefore, in this study we use $\Delta\sigma_0 \leq 0.03\,\mathrm{kg\,m^{-3}}$ to estimate the MLD in the Southern Ocean.

We then repeat subduction calculations using MLD criteria of $\Delta\sigma_0 \leq 0.03\,\mathrm{kg\,m^{-3}}$ and $\Delta\sigma_0 \leq 0.125\,\mathrm{kg\,m^{-3}}$ to examine the uncertainties in subduction rate that originate from our choices in the MLD fields (Figs. B2a,b). The annual mean subduction rate obtained within the density range $\sigma_0 = [26.5\text{–}27.1]\,\mathrm{kg\,m^{-3}}$ shows that these two MLD criteria yield essentially the same interannual variations in subduction rate, except for some slight differences in years of 2012, 2014 and 2016 in its magnitude.

b. Geostrophic velocity

To test the uncertainties that arise from the velocity fields applied, we repeat our calculations using the velocity fields derived from a reference level of no motion at 1950, 1750, and 1500 m, as well as the climatologically annual mean geostrophic velocity at 1950 m taken from Gray and Riser (2014) and at 1000 m from Lebedev et al. (2007). The results obtained show that the choice of geostrophic velocity fields has little impact on the resulting subduction estimates within the density range $\sigma_0 = [26.5\text{–}27.1]\,\mathrm{kg\,m^{-3}}$ (e.g., same interannual variations in Fig. B2c), except for slight differences in magnitude (<8%, Fig. B2c). Thus, our subduction estimates are robust relative to the choice of the MLD and geostrophic velocity fields.

The subduction rates presented in this paper use the mean of the subduction rates calculated using the velocity fields derived from 1) the 1950 m level of no motion, 2) Gray and Riser (2014), and 3) Lebedev et al. (2007), while using the MLD threshold criterion of $\Delta\sigma_0 \leq 0.03\,\mathrm{kg\,m^{-3}}$. In the above, the subduction rates in Fig. B2 were integrated within the density range $\sigma_0 = [26.5\text{–}27.1]\,\mathrm{kg\,m^{-3}}$ for the method validation (gray bars in Fig. 5a). The potential density, low PV, temperature, and salinity constraints from the SAMW definition were further imposed in the computation to focus on the subduction flux only for SAMW (purple bars in Fig. 5a).

APPENDIX C

Interannual Variability in SAMW Formation

Recent studies have shown that the increasing SAMW subduction rate across the Southern Ocean dominates the observed increase in total SAMW volume during the Argo period, influencing the ocean uptake and storage of heat as well as carbon (Gao et al. 2018; Kolodziejczyk et al. 2019; Qu et al. 2020). The interannual variation of annual subduction is closely tied to variability in the winter MLD (Kwon 2013;

JOBNAME: JPO 00#00 2021 PAGE: 17 SESS: 8 OUTPUT: Tue Aug 24 08:17:11 2021 Total No. of Pages: 22
/ams/jpo/0/jpoD200174

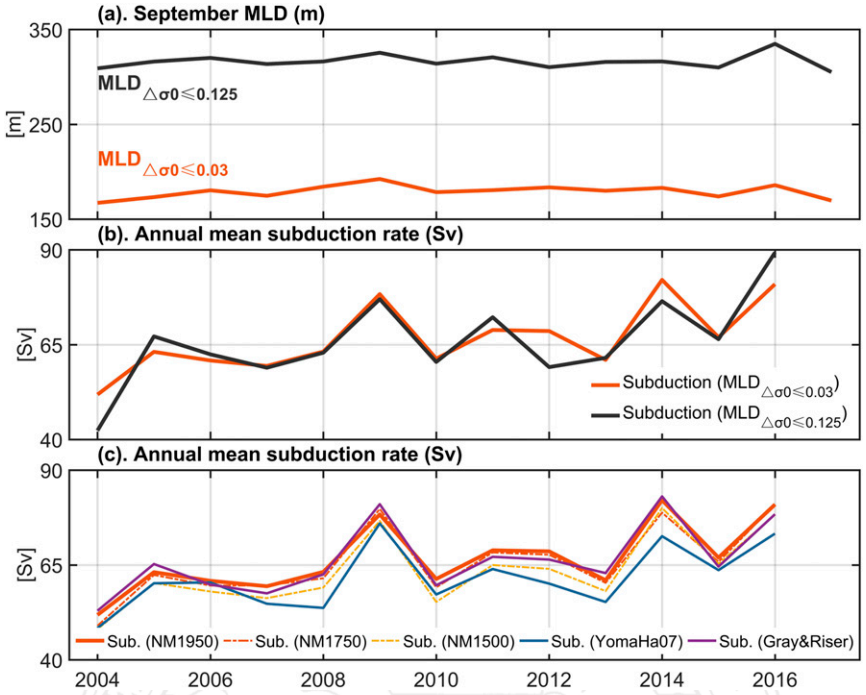

FIG. B2. (a) Time series of the September MLD (m) averaged within the density range σ_0 = [26.5–27.1] kg m^{-3}. Red and black solid lines represent the MLD calculated using MLD criteria of $\Delta\sigma_0 \leq 0.03$ and $\Delta\sigma_0 \leq 0.125$ kg m^{-3}, respectively. (b) Annual mean subduction rate within the density range σ_0 = [26.5–27.1] kg m^{-3} calculated using MLD criteria of $\Delta\sigma_0 \leq 0.03$ kg m^{-3} (red solid line) and $\Delta\sigma_0 \leq 0.125$ kg m^{-3} (black solid line). (c) Annual mean subduction rate within the density range σ_0 = [26.5–27.1] kg m^{-3} calculated using the geostrophic velocity fields derived from a reference level of no motion at 1950 (red solid line), 1750 (red dashed line), and 1500 m (yellow dashed line), as well as the reference velocity at 1950 m taken from Gray and Riser (2014) (purple solid line) and at 1000 m from Lebedev et al. (2007) (blue solid line). All subduction estimates in (c) are based on the same MLD criterion of $\Delta\sigma_0 \leq 0.03$ kg m^{-3}.

Qu et al. 2020) since the deep winter mixed layer is responsible for connecting the surface with intermediate layers and thus exchanges between them (section 6). Combining with section 6, we also find that interannual variability in $SAMW_{ML}$ volume increase is strongly correlated with the air–sea formation rate averaged over the surface buoyancy loss period of April–August (Figs. 8a,b), with a positive correlation coefficient of 0.71 (Figs. C1a,b). On the other hand, interannual variability in $SAMW_{ML}$ volume decrease and the monthly subduction rate averaged over August–October (Figs. 8b,c) show a strong negative correlation coefficient of −0.98 (Figs. C1b,c), while the $SAMW_{INT}$ volume increase is closely tied to the monthly subduction over the same period (correlation coefficient of 0.82, Figs. C1c,d). The strong correlation between interannual variability in SAMW volume change and SAMW formation estimates supports the results of the seasonal cycle of SAMW formation presented in section 6.

This study also adapted a volumetric method from Davis et al. (2011) to measure the annually averaged volume formation (V_i^{for}) and destruction (V_i^{des}) rates of SAMW, namely,

$$V_i^{for} = (V_i^{max} - V_i^{min})/\Delta T, \quad \text{(C1)}$$

and

$$V_i^{des} = (V_i^{max} - V_{i+1}^{min})/\Delta T, \quad \text{(C2)}$$

respectively (blue bars in Figs. C2a,b). Here V_i^{max} is the volume maximum in year i, V_i^{min} and V_{i+1}^{min} are the volume minima in years i and $i + 1$, respectively, and ΔT is a 1-yr time increment. The resulting annual formation and destruction rates in the volume of $SAMW_{ML}$ are closely correlated (0.99) and share the same long-term average magnitude (~150 Sv). The annual formation and destruction rates in the volume of $SAMW_{INT}$ also share the same magnitude (~100 Sv) but are not highly correlated (0.49). By comparing estimates from the volumetric method with the SAMW formation estimates of air–sea formation and Lagrangian subduction, about 80% of the annual volume formation of $SAMW_{ML}$ can be accounted for by air–sea interaction during the surface buoyancy loss period (124 ± 13 Sv, Fig. C2a), while over a half of the annual volume formation of $SAMW_{INT}$ can be explained by annual mean subduction (42 ± 7 Sv, Fig. C2b), with a correlation coefficient of 0.62.

Note that historical ocean reanalysis data prior to Argo were also analyzed in this study, using the Simple Ocean Data

JOBNAME: JPO 00#00 2021 PAGE: 18 SESS: 8 OUTPUT: Tue Aug 24 08:17:11 2021 Total No. of Pages: 22
/ams/jpo/0/jpoD200174

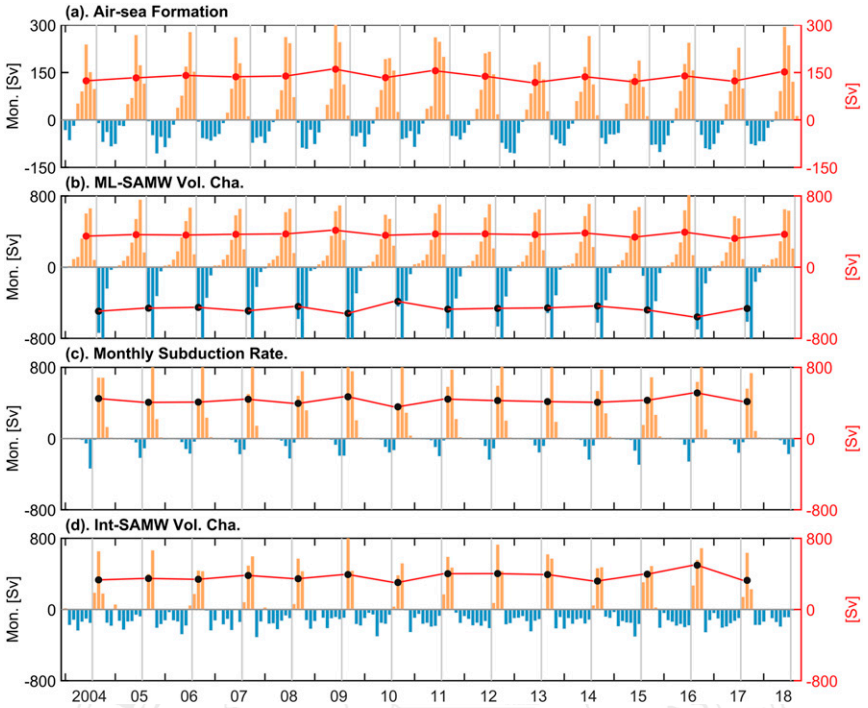

FIG. C1. (a) Monthly air–sea formation rate (bars; Sv), and the air–sea formation rate averaged over April–August (red line; Sv), (b) Monthly volume change of $SAMW_{ML}$ (bars; Sv), and the mean value averaged over April–August (red line with red dots; Sv) and over August–October (red line with black dots; Sv). (c) Monthly subduction rate (bars; Sv) derived from Eq. (1), and the subduction rate averaged over August–October (red line with black dots; Sv). Gray lines in (c) and (d) represent the position of August, in which the detrainment starts to occur. (d) Monthly volume change of $SAMW_{INT}$ (bars; Sv) and the mean value averaged over August–October (red line with black dots; Sv). All estimates are constrained by the SAMW criteria shown in Table 1 for consistency.

Assimilation (SODA) ocean–sea ice reanalysis. However, unrealistically large year-to-year variations in MLD and SAMW volume give us limited confidence in any long-term (pre-Argo) record of the metrics analyzed in this paper (Figs. C2c,d). For example, the standard deviation in the annual mean SAMW volume is $\sim 2 \times 10^{15}$ m^3 pre-Argo, but only $\sim 3 \times 10^{14}$ m^3 once the Argo hydrographic data are available to better constrain this metric. This is virtually certain to be due to data sparsity pre-Argo, and not any abrupt shift in Southern Ocean climate variability. Thus, the focus of this study is limited to the Argo era.

APPENDIX D

SAMW Formation by Air–Sea Buoyancy Fluxes

The surface water-mass transformation rate F and formation rate ΔF, resulting from air–sea buoyancy fluxes, are calculated (e.g., Maze et al. 2009) as

$$F(\sigma_0, t) = \frac{1}{g\Delta\sigma}\int\int_{\sigma_0-\frac{\Delta\sigma}{2}}^{\sigma_0+\frac{\Delta\sigma}{2}} B_{\text{net}}\, d\mathcal{A}_s \qquad \text{(D1)}$$

and

$$\Delta F(\sigma_0, t) = F\left(\sigma_0 - \frac{\Delta\sigma}{2}\right) - F\left(\sigma_0 + \frac{\Delta\sigma}{2}\right), \qquad \text{(D2)}$$

respectively. Here, $\mathcal{A}_s$ is the instantaneous surface area of the outcrop window within $\sigma \pm (\Delta\sigma/2)$, positive F corresponds to transformation toward increasing density, and ΔF is the convergence of F and quantifies the formation or destruction of water in a density class. The buoyancy flux used in Eq. (D1) is defined as

$$B_{\text{net}} = \frac{g\alpha}{C_w} H_{\text{in}} + g\beta\bar{\rho}S_m(P - E), \qquad \text{(D3)}$$

where α, C_w, β, S_m, and $\bar{\rho}$ represent the thermal expansion coefficient, the heat capacity of seawater, the haline contraction coefficient, the averaged S_A over the mixed layer, and the mean ocean density, respectively. Here, the net surface heat flux H_{in} consists of the sum of latent and sensible heat fluxes as well as shortwave and longwave radiation. The surface freshwater flux $P - E$ is taken as the difference between precipitation P and evaporation E. Here, $B_{\text{net}} > 0$ represents a buoyancy loss out of the ocean surface layer. Effects of shortwave radiation penetration change WMT can be up to

JOBNAME: JPO 00#00 2021 PAGE: 19 SESS: 8 OUTPUT: Tue Aug 24 08:17:12 2021 Total No. of Pages: 22
/ams/jpo/0/jpoD200174

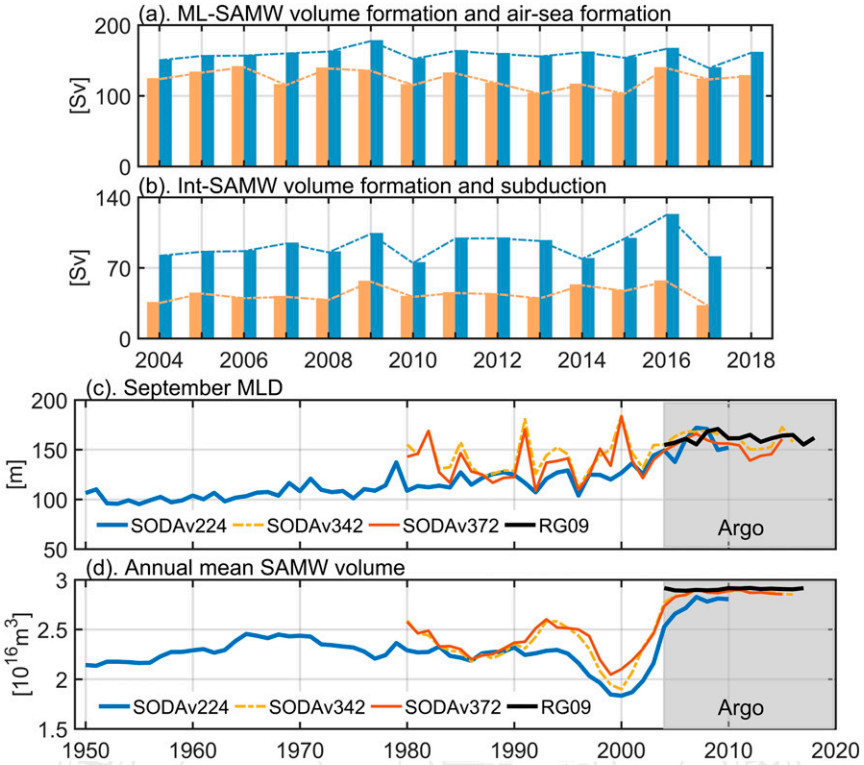

FIG. C2. (a) Formation of $SAMW_{ML}$ (Sv) during the period 2004–18. Blue bars and dashed line indicate the annual volume formation of $SAMW_{ML}$ using Eq. (C1), yellow represents the SAMW formation by air–sea fluxes averaged over the surface buoyancy loss period. (b) Formation of $SAMW_{INT}$ (Sv). Blue bars and dashed lines indicate the annual volume formation of $SAMW_{INT}$ using Eq. (C1), and yellow bars and lines denote the SAMW formation by annual mean subduction rate based on Eq. (4). (c),(d) Time series of the September MLD (m) and annual mean SAMW volume (10^{16} m^3) from 1950 to 2018 over the whole Southern Ocean using the gridded RG09 Argo product and SODA products (SODA version 2.2.4, 3.4.2, and 3.7.2). Gray shading represents the Argo era since 2004.

20%–50% in regions with shallow mixed layers (Iudicone et al. 2011, Groeskamp and Iudicone 2018); however, for SAMW this effect is relatively small (Fig. 3c of Groeskamp and Iudicone 2018; Lee et al. 2011), and this is therefore not included in this study. The freshwater input from sea ice melt also plays an important role in the formation and destruction of SAMW (e.g., Abernathey et al. 2016; Groeskamp et al. 2016; Cerovečki et al. 2019), but is not considered in this study due to the limitation of the dataset used.

Note here we impose the low PV, temperature, and salinity constraints from the SAMW definition when estimating the SAMW formation due to air–sea buoyancy fluxes. Only the buoyancy fluxes that impact on surface temperatures and salinities within the SAMW definition are counted in our WMT calculation. Since the buoyancy fluxes that impact outside of the SAMW temperature and salinity limits could also transfer water parcels into SAMW, minor uncertainties could be induced by ignoring these edge effects in our monthly WMT estimates. We use a fixed density range of σ_0 = [26.5–27.1] kg m^{-3} to encompasses all the SAMW density ranges in Southern Ocean sectors. To compare with the air–sea formation rate integrated within σ_0 = [26.5–27.1] kg m^{-3}, the air–sea formation rates derived from fixed density ranges of σ_0 = [26.5–27.0], [26.6–27.0], and [26.6–27.1] kg m^{-3} are shown in Fig. 7c. Only slight differences can be found between the air–sea formation rates integrated within the σ_0 = [26.5–27.1] kg m^{-3} density layer and the other three density ranges, suggesting the results obtained are robust to this choice.

REFERENCES

Abernathey, R. P., I. Cerovecki, P. R. Holland, E. Newsom, M. Mazloff, and L. D. Talley, 2016: Water-mass transformation by sea ice in the upper branch of the Southern Ocean overturning. *Nat. Geosci.*, **9**, 596–601, https://doi.org/10.1038/ngeo2749.

Barker, P. M., and T. J. McDougall, 2017: Stabilizing hydrographic profiles with minimal change to the water masses. *J. Atmos. Oceanic Technol.*, **34**, 1935–1945, https://doi.org/10.1175/JTECH-D-16-0111.1.

Bostock, H. C., P. J. Sutton, M. J. M. Williams, and B. N. Opdyke, 2013: Reviewing the circulation and mixing of Antarctic Intermediate Water in the south Pacific using evidence from

geochemical tracers and Argo float trajectories. *Deep-Sea Res. I*, **73**, 84–98, https://doi.org/10.1016/j.dsr.2012.11.007.

Canuto, V. M., and Y. Cheng, 2019: ACC subduction by mesoscales. *J. Phys. Oceanogr.*, **49**, 3263–3272, https://doi.org/10.1175/JPO-D-19-0043.1.

Cerovečki, I., and M. R. Mazloff, 2016: The spatiotemporal structure of diabatic processes governing the evolution of Subantarctic Mode Water in the Southern Ocean. *J. Phys. Oceanogr.*, **46**, 683–710, https://doi.org/10.1175/JPO-D-14-0243.1.

——, L. D. Talley, M. R. Mazloff, and G. Maze, 2013: Subantarctic Mode Water formation, destruction, and export in the eddy-permitting Southern Ocean State Estimate. *J. Phys. Oceanogr.*, **43**, 1485–1511, https://doi.org/10.1175/JPO-D-12-0121.1.

——, A. J. S. Meijers, M. R. Mazloff, S. T. Gille, V. M. Tamsitt, and P. R. Holland, 2019: The effects of enhanced sea ice export from the Ross Sea on recent cooling and freshening of the southeast Pacific. *J. Climate*, **32**, 2013–2035, https://doi.org/10.1175/JCLI-D-18-0205.1.

Cushman-Roisin, B., 1987: Subduction. *Dynamics of the Oceanic Surface Mixed-Layer*, P. Müller and D. Henderson, Eds., Hawaii Institute of Geophysical Special Publications, 181–196.

Davis, X. J., L. M. Rothstein, W. K. Dewar, and D. Menemenlis, 2011: Numerical investigations of seasonal and interannual variability of North Pacific subtropical mode water and its implications for Pacific climate variability. *J. Climate*, **24**, 2648–2665, https://doi.org/10.1175/2010JCLI3435.1.

de Boyer Montégut, C., G. Madec, A. S. Fischer, A. Lazar, and D. Iudicone, 2004: Mixed layer depth over the global ocean: An examination of profile data and a profile-based climatology. *J. Geophys. Res.*, **109**, C12003, https://doi.org/10.1029/2004JC002378.

de Lavergne, C., and Coauthors, 2020: A parameterization of local and remote tidal mixing. *J. Adv. Model. Earth Syst.*, **12**, e2020MS002065, https://doi.org/10.1029/2020MS002065.

Dong, S., J. Sprintall, S. T. Gille, and L. Talley, 2008: Southern ocean mixed-layer depth from Argo float profiles. *J. Geophys. Res.*, **113**, C06013, https://doi.org/10.1029/2006JC004051.

Donners, J., S. S. Drijfhout, and W. Hazeleger, 2005: Water mass transformation and subduction in the South Atlantic. *J. Phys. Oceanogr.*, **35**, 1841–1860, https://doi.org/10.1175/JPO2782.1.

AU8

Downes, S. M., N. L. Bindoff, and S. R. Rintoul, 2009: Impacts of climate change on the subduction of mode and intermediate water masses in the Southern Ocean. *J. Climate*, **22**, 3289–3302, https://doi.org/10.1175/2008JCLI2653.1.

——, ——, and ——, 2010: Changes in the subduction of Southern Ocean water masses at the end of the twenty-first century in eight IPCC models. *J. Climate*, **23**, 6526–6541, https://doi.org/10.1175/2010JCLI3620.1.

——, A. S. Budnick, J. L. Sarmiento, and R. Farneti, 2011a: Impacts of wind stress on the Antarctic Circumpolar Current fronts and associated subduction. *Geophys. Res. Lett.*, **38**, L11605, https://doi.org/10.1029/2011GL047668.

——, A. Gnanadesikan, S. M. Griffies, and J. L. Sarmiento, 2011b: Water mass exchange in the Southern Ocean in coupled climate models. *J. Phys. Oceanogr.*, **41**, 1756–1771, https://doi.org/10.1175/2011JPO4586.1.

Evans, D. G., J. D. Zika, A. C. Naveira Garabato, and A. J. G. Nurser, 2014: The imprint of Southern Ocean overturning on seasonal water mass variability in Drake Passage. *J. Geophys. Res. Oceans*, **119**, 7987–8010, https://doi.org/10.1002/2014JC010097.

——, ——, ——, and ——, 2018: The cold transit of Southern Ocean upwelling. *Geophys. Res. Lett.*, **45**, 13 386–13 395, https://doi.org/10.1029/2018GL079986.

Gao, L., S. R. Rintoul, and W. Yu, 2018: Recent wind-driven change in Subantarctic Mode Water and its impact on ocean heat storage. *Nat. Climate Change*, **8**, 58–63, https://doi.org/10.1038/s41558-017-0022-8.

Gray, A. R., and S. C. Riser, 2014: A global analysis of Sverdrup balance using absolute geostrophic velocities from Argo. *J. Phys. Oceanogr.*, **44**, 1213–1229, https://doi.org/10.1175/JPO-D-12-0206.1.

Groeskamp, S., and D. Iudicone, 2018: The effect of air-sea flux products, shortwave radiation depth penetration, and albedo on the upper ocean overturning circulation. *Geophys. Res. Lett.*, **45**, 9087–9097, https://doi.org/10.1029/2018GL078442.

——, R. P. Abernathey, and A. Klocker, 2016: Water mass transformation by cabbeling and thermobaricity. *Geophys. Res. Lett.*, **43**, 10 835–10 845, https://doi.org/10.1002/2016GL070860.

——, B. M. Sloyan, J. D. Zika, and T. J. McDougall, 2017: Mixing inferred from an ocean climatology and surface fluxes. *J. Phys. Oceanogr.*, **47**, 667–687, https://doi.org/10.1175/JPO-D-16-0125.1.

——, P. M. Barker, T. J. McDougall, R. P. Abernathey, and S. Griffies, 2019a: VENM: An algorithm to accurately calculate neutral slopes and gradients. *J. Adv. Model. Earth Syst.*, **11**, 1917–1939, https://doi.org/10.1029/2019MS001613.

——, S. Griffies, D. Iudicone, R. Marsh, G. Nurser, and J. Zika, 2019b: The water mass transformation framework for ocean physics and biogeochemistry. *Annu. Rev. Mar. Sci.*, **11**, 271–305, https://doi.org/10.1146/annurev-marine-010318-095421.

——, J. H. LaCasce, T. J. McDougall, and M. Rogé, 2020: Full-depth global estimates of ocean mesoscale eddy mixing from observations and theory. *Geophys. Res. Lett.*, **47**, e2020GL089425, https://doi.org/10.1029/2020GL089425.

Hanawa, K., and L. D. Talley, 2001: Mode waters. *Ocean Circulation and Climate: A 21st Century Perspective*, G. Siedler et al., Eds., International Geophysics Series, Vol. 103, Academic Press, 373–386.

Herraiz-Borreguero, L., and S. Rintoul, 2011: Subantarctic Mode Water: Distribution and circulation. *Ocean Dyn.*, **61**, 103–126, https://doi.org/10.1007/s10236-010-0352-9.

Hiraike, Y., Y. Tanaka, and H. Hasumi, 2016: Subduction of Pacific Antarctic Intermediate Water in an eddy-resolving model. *J. Geophys. Res. Oceans*, **121**, 133–147, https://doi.org/10.1002/2015JC010802.

IOC, SCOR, and IAPSO, 2010: The International Thermodynamic Equation of Seawater—2010: Calculation and use of thermodynamic properties. Intergovernmental Oceanographic Commission, Manuals and Guides 56, 220 pp., http://www.teos-10.org/pubs/TEOS-10_Manual.pdf.

Iudicone, D., S. Speich, G. Madec, and B. Blanke, 2008: The global conveyor belt from a Southern Ocean perspective. *J. Phys. Oceanogr.*, **38**, 1401–1425, https://doi.org/10.1175/2007JPO3525.1.

——, K. B. Rodgers, I. Stendardo, O. Aumont, G. Madec, L. Bopp, O. Mangoni, and M. Ribera d'Alcala', 2011: Water masses as a unifying framework for understanding the Southern Ocean Carbon Cycle. *Biogeosciences*, **8**, 1031–1052, https://doi.org/10.5194/bg-8-1031-2011.

Jones, D. C., A. J. S. Meijers, E. Shuckburgh, J.-B. Sallée, P. Haynes, E. K. McAufield, and M. R. Mazloff, 2016: How does Subantarctic Mode Water ventilate the Southern

Hemisphere subtropics? *J. Geophys. Res. Oceans*, **121**, 6558–6582, https://doi.org/10.1002/2016JC011680.

Karstensen, J., and D. Quadfasel, 2002a: Water subducted into the Indian Ocean subtropical gyre. *Deep-Sea Res. II*, **49**, 1441–1457, https://doi.org/10.1016/S0967-0645(01)00160-6.

——, and ——, 2002b: Formation of Southern Hemisphere thermocline waters: Water mass conversion and subduction. *J. Phys. Oceanogr.*, **32**, 3020–3038, https://doi.org/10.1175/1520-0485(2002)032<3020:FOSHTW>2.0.CO;2.

Koch-Larrouy, A., R. Morrow, T. Penduff, and M. Juzal, 2010: Origin and mechanism of Subantarctic Mode Water formation and transformation in the southern Indian Ocean. *Ocean Dyn.*, **60**, 563–583, https://doi.org/10.1007/s10236-010-0276-4.

Kolodziejczyk, N., W. Llovel, and E. Portela, 2019: Interannual variability of upper ocean water masses as inferred from Argo array. *J. Geophys. Res. Oceans*, **124**, 6067–6085, https://doi.org/10.1029/2018JC014866.

Kwon, E. Y., 2013: Temporal variability of transformation, formation, and subduction rates of upper Southern Ocean waters. *J. Geophys. Res. Oceans*, **118**, 6285–6302, https://doi.org/10.1002/2013JC008823.

——, S. M. Downes, J. L. Sarmiento, R. Farneti, and C. Deutsch, 2013: Role of the seasonal cycle in the subduction rates of upper Southern Ocean waters. *J. Phys. Oceanogr.*, **43**, 1096–1113, https://doi.org/10.1175/JPO-D-12-060.1.

Lebedev, K. V, H. Yoshinari, N. A. Maximenko, and P. W. Hacker, 2007: YoMaHa'07: Velocity data assessed from trajectories of Argo floats at parking level and at the sea surface. IPRC Tech. Note 4(2), 16 pp., http://apdrc.soest.hawaii.edu/projects/Argo/data/Documentation/YoMaHa070612.pdf.

Lee, M. M., A. J. G. Nurser, I. Stevens, and J. B. Sallée, 2011: Subduction over the southern Indian Ocean in a high-resolution atmosphere–ocean coupled model. *J. Climate*, **24**, 3830–3849, https://doi.org/10.1175/2011JCLI3888.1.

Liu, C., and Z. Wang, 2014: On the response of the global subduction rate to global warming in coupled climate models. *Adv. Atmos. Sci.*, **31**, 211–218, https://doi.org/10.1007/s00376-013-2323-9.

Liu, L. L., and R. X. Huang, 2012: The global subduction/obduction rates: Their interannual and decadal variability. *J. Climate*, **25**, 1096–1115, https://doi.org/10.1175/2011JCLI4228.1.

Lu, Y., L. D. Talley, I. Cerovečki, S. T. Gille, S-P. Xie, M. R. Mazloff, Q. Liu, and Y. Zhang, 2020: Southern Ocean deep mixed layers and ventilated mode waters: Eastward-propagating interannual climate variability. *Nat. Commun.*, submitted.

AU9

Marshall, J. C., A. J. G. Nurser, and R. G. Williams, 1993: Inferring the subduction rate and period over the North Atlantic. *J. Phys. Oceanogr.*, **23**, 1315–1329, https://doi.org/10.1175/1520-0485(1993)023<1315:ITSRAP>2.0.CO;2.

——, D. Jamous, and J. Nilsson, 1999: Reconciling thermodynamic and dynamic methods of computation of water-mass transformation rates. *Deep-Sea Res. I*, **46**, 545–572, https://doi.org/10.1016/S0967-0637(98)00082-X.

Maze, G., G. Forget, M. Buckley, J. Marshall, and I. Cerovečki, 2009: Using transformation and formation maps to study the role of air–sea heat fluxes in North Atlantic Eighteen Degree Water formation. *J. Phys. Oceanogr.*, **39**, 1818–1835, https://doi.org/10.1175/2009JPO3985.1.

McCartney, M. S., 1977: Subantarctic mode water. *A Voyage of Discovery: George Deacon 70th Anniversary Volume*, M. V. Angel, Ed., Pergamon Press, 103–119.

——, 1982: The subtropical recirculation of mode water. *J. Mar. Res.*, **40**, 427–464.

McDougall, T. J., 2003: Potential enthalpy: A conservative oceanic variable for evaluating heat content and heat fluxes. *J. Phys. Oceanogr.*, **33**, 945–963, https://doi.org/10.1175/1520-0485(2003)033<0945:PEACOV>2.0.CO;2.

——, D. R. Jackett, F. J. Millero, R. Pawlowicz, and P. M. Barker, 2012: A global algorithm for estimating Absolute Salinity. *Ocean Sci.*, **8**, 1123–1134, https://doi.org/10.5194/osd-6-215-2009.

Meijers, A. J. S., I. Cerovečki, B. A. King, and V. Tamsitt, 2019: A see-saw in Pacific Subantarctic Mode Water formation driven by atmospheric modes. *Geophys. Res. Lett.*, **46**, 13 152–13 160, https://doi.org/10.1029/2019GL085280.

Monterey, G., and S. Levitus, 1997: Seasonal variability of mixed layer depth for the world ocean. NOAA Atlas NESDIS 14, 102 pp., ftp://ftp.nodc.noaa.gov/pub/data.nodc/woa/PUBLICATIONS/Atlas14.pdf.

Nishikawa, S., H. Tsujino, K. Sakamoto, and H. Nakano, 2013: Diagnosis of water mass transformation and formation rates in a high-resolution GCM of the North Pacific. *J. Geophys. Res. Oceans*, **118**, 1051–1069, https://doi.org/10.1029/2012JC008116.

Nurser, A. J. G., R. Marsh, and R. G. Williams, 1999: Diagnosing water mass formation from air–sea fluxes and surface mixing. *J. Phys. Oceanogr.*, **29**, 1468–1487, https://doi.org/10.1175/1520-0485(1999)029<1468:DWMFFA>2.0.CO;2.

Obata, A., J. Ishizaka, and M. Endoh, 1996: Global verification of critical depth theory for phytoplankton bloom with climatological in situ temperature and satellite ocean color data. *J. Geophys. Res.*, **101**, 20 657–20 667, https://doi.org/10.1029/96JC01734.

Portela, E., N. Kolodziejczyk, C. Maes, and V. Thierry, 2020: Interior water-mass variability in the Southern-Hemisphere oceans during the last decade. *J. Phys. Oceanogr.*, **50**, 361–381, https://doi.org/10.1175/JPO-D-19-0128.1.

Qiu, B., and R. X. Huang, 1995: Ventilation of the North Atlantic and North Pacific: Subduction versus obduction. *J. Phys. Oceanogr.*, **25**, 2374–2390, https://doi.org/10.1175/1520-0485(1995)025<2374:VOTNAA>2.0.CO;2.

Qu, T., S. Gao, and R. A. Fine, 2020: Variability of the Sub-Antarctic Mode Water subduction rate during the Argo period. *Geophys. Res. Lett.*, **47**, e2020GL088248, https://doi.org/10.1029/2020GL088248.

Ridgway, K. R., and J. R. Dunn, 2007: Observational evidence for a Southern Hemisphere oceanic supergyre. *Geophys. Res. Lett.*, **34**, L13612, https://doi.org/10.1029/2007GL030392.

Rintoul, S. R., and M. H. England, 2002: Ekman transport dominates local air–sea fluxes in driving variability of Subantarctic Mode Water. *J. Phys. Oceanogr.*, **32**, 1308–1321, https://doi.org/10.1175/1520-0485(2002)032<1308:ETDLAS>2.0.CO;2.

Roemmich, D., and J. Gilson, 2009: The 2004–2008 mean and annual cycle of temperature, salinity, and steric height in the global ocean from the Argo Program. *Prog. Oceanogr.*, **82**, 81–100, https://doi.org/10.1016/j.pocean.2009.03.004.

——, J. Church, J. Gilson, D. Monselesan, P. Sutton, and S. Wijffels, 2015: Unabated planetary warming and its ocean structure since 2006. *Nat. Climate Change*, **5**, 240–245, https://doi.org/10.1038/nclimate2513.

Sallée, J. B., and S. R. Rintoul, 2011: Parameterization of eddy-induced subduction in the Southern Ocean surface layer. *Ocean Modell.*, **39**, 146–153, https://doi.org/10.1016/j.ocemod.2011.04.001.

JOBNAME: JPO 00#00 2021 PAGE: 22 SESS: 8 OUTPUT: Tue Aug 24 08:17:13 2021 Total No. of Pages: 22
/ams/jpo/0/jpoD200174

——, K. Speer, S. R. Rintoul, and S. Wijffels, 2010a: Southern Ocean thermocline ventilation. *J. Phys. Oceanogr.*, **40**, 509–529, https://doi.org/10.1175/2009JPO4291.1.

——, ——, and ——, 2010b: Zonally asymmetric response of the Southern Ocean mixed-layer depth to the Southern Annular Mode. *Nat. Geosci.*, **3**, 273–279, https://doi.org/10.1038/ngeo812.

Sloyan, B. M., and S. R. Rintoul, 2001: The Southern Ocean limb of the global deep overturning circulation. *J. Phys. Oceanogr.*, **31**, 143–173, https://doi.org/10.1175/1520-0485(2001)031<0143:TSOLOT>2.0.CO;2.

Tamsitt, V., I. Cerovečki, S. A. Josey, S. T. Gille, and E. Schulz, 2020: Mooring observations of air-sea heat fluxes in two Subantarctic Mode Water formation regions. *J. Climate*, **33**, 2757–2777, https://doi.org/10.1175/JCLI-D-19-0653.1.

Walin, G., 1982: On the relation between sea-surface heat flow and thermal circulation in the ocean. *Tellus*, **34**, 187–195, https://doi.org/10.3402/tellusa.v34i2.10801.

Williams, R. G., 1991: The role of the mixed layer in setting the potential vorticity of the main thermocline. *J. Phys. Oceanogr.*, **21**, 1803–1814, https://doi.org/10.1175/1520-0485(1991)021<1803:TROTML>2.0.CO;2.

Wong, A. P. S., 2005: Subantarctic Mode Water and Antarctic Intermediate Water in the south Indian Ocean based on profiling float data 2000–2004. *J. Mar. Res.*, **63**, 789–812, https://doi.org/10.1357/0022240054663196.

Woods, J. D., 1985: The physics of thermocline ventilation. *Coupled Ocean–Atmosphere Models*, J. C. J. Nihoul, Ed., Elsevier Oceanography Series, Vol. 40, Elsevier, 543–590, https://doi.org/10.1016/S0422-9894(08)70730-X.